MASTER'S FINAL THESIS

Master's degree in Chemical Engineering – Smart Chemical Factories

DOPING OF SOLUTION-PROCESSED TWO-DIMENSIONAL TRANSITION METAL DICHALCOGENIDES

Written Report

Author: Marc Esteve Cantero

Director: Raul Benítez Iglesias

Department: ESAII

Date: June 2021

DOPING OF SOLUTION-PROCESSED TWO-DIMENSIONAL TRANSITION METAL DICHALCOGENIDES

PRÉSENTÉE LE 5 JUILLET 2021

FACULTE DES SCIENCES DE BASE

LABORATOIRE D'INGENIERIE MOLECULAIRE DES NANOMATERIAUX OPTOELECTRONIQUES

MASTERS EN CHIMIE ET GENIE CHIMIQUE

ÉCOLE POLYTECHNIQUE FÉDÉRALE DE LAUSANNE (EPFL)

par

Marc ESTEVE CANTERO

2021

Acknowledgements

Thanks to the prof. Kevin Sivula and to the PhD student Rebekah Wells for giving me the opportunity of developing my Master's Thesis at LIMNO and supporting me when I needed it. Also, to the whole LIMNO group for welcoming me and always being keen to help.

I would also like to thank my parents for all the support given from Barcelona and mention my exchange community that I have made in Switzerland, which definitely has helped me to make the most of this experience.

Abstract

Semiconducting transition metal dichalcogenides (TMDs) such as MoS_2, WSe_2 or WS_2 have attracted a lot of interest in recent years because of their outstanding optoelectronic properties including tunable bandgap or strong light absorption in the visible range, even at sub-micrometer thickness. Furthermore, doping these materials with transition metal atoms is an approach which can additionally modify a TMDs' optoelectronic properties and therefore could enable these TMDs to take part in new applications.

Indeed, one method to exfoliate TMD materials is the electrochemical intercalation of TMDs with THA^+ molecules. Recently this method was altered to make it more scalable, using annealed pellets made from commercially available powder. This method is readily adaptable such that bulk TMDs are doped in the annealing phase before being exfoliated into doped 2D TMD nanoflakes.

In this work we present an extensive study regarding p-type doping of MoS_2 with Niobium (Nb) for different atomic concentrations. We confirm the incorporation of the dopant agent to the TMD crystal lattice and observe consequential changes in the optoelectronic properties of the resulting nanoflakes. Besides, from 0.75% Nb doping the intrinsic n-type MoS_2 displays ambipolar due to the p-type behavior added by Nb atoms. Consequently, $NbMoS_2$ shows promise as a building block of ultra-thin ambipolar field effect transistors (FETs).

We follow up with the incorporation of n-type dopant agent Rhenium (Re) as preliminary story. Here, Re is also confirmed to enter at MoS_2 crystal structure. However, as it stands 0.5% and 1% Re doping to MoS_2 are not beneficial for PEC performance of this material.

Finally, we show that this method can also be used for other TMDs such as p-type WSe_2 and n-type WS_2, showcasing the universality of this method. Here, dopant agent incorporation to the TMDs crystal lattices is also confirmed and therefore optoelectronic properties of WSe_2 and WS_2 are also demonstrated to change because of Nb addition.

In summary, we successfully dope 2D TMD materials using a scalable, solution-processable method and we show that these doped materials have potential in future ultrathin optoelectronic devices.

Keywords

Transition metal dichalcogenide, doping, bandgap, optoelectronic properties, MoS2, WSe2, WS2, Nb, Re, electrochemical intercalation, two dimensional, ambipolar

List of abbreviations

2D	Two-Dimensional
CVD	Chemical Vapour Deposition
FET	Field Effect Transistor
HER	Hydrogen Evolution Reaction
ICP-MS	Inductively Couple Plasma Mass Spectrometry
LLISA	Liquid-Liquid Interfacial Solvent Assisted
LSV	Linear Scan Voltammetry
OCP	Open Circuit Potential
OER	Oxygen Evolution Reaction
PEC	Photo Electrochemical Cells
PL	Photoluminescence
TBAFP	Tetra-n-butylammonium fluoride
THAB	Tetraheptylammoniumbromide
TMD	Transition Metal Dichalcogenide
SEM	Scanning Electron Microscope
UPS	Ultraviolet Photoelectron Spectroscopy
UV-VIS	Ultra Violet-Visible
VdW	Van der Waals
XPS	X-Ray Photoelectron Spectroscopy
XRD	X-Ray Diffraction

Contents

List of Figures

Chapter 1 Introduction

Two-dimensional (2D) materials have aroused a lot of interest in recent years since unique optical and electronical properties have been reported on them[1-4]. Among them, transition metal dichalcogenides (TMDs) stand out because they are earth abundant, nontoxic and exhibit unique and tunable optoelectronic properties[5]. All these properties make TMDs suitable for electronic and optoelectronic devices as transistors[6], sensors[7,8], batteries[9] and also make them promising photocatalysts[10,11,12] or photoelectrodes in photoelectrochemical (PEC) cells for water splitting[13].

1.1 Overview of TMDs

TMDs consist of a MX_2 structure, where M is a transition element (Mo, W…) and X is a chalcogen atom (S, Se...)[14]. The metal atom is located between the two chalcogenide atoms held together by covalent bonding[15]. These individual layers are held together by weak Van der Vaals forces (Figure 1b), which gives the material a bulk shape and layered structure[16]. Regarding structural phases of TMDs, they can be mostly found in trigonal prismatic structure (2H) or octahedral (1T) and less commonly in dimerized (1T') phase[14] (Figure 1a). The thermodynamically stable phase will be defined depending on the combination of transition metal and chalcogen atoms, so for TMDs formed by a Group VI transition metal (Mo or W) and a chalcogen (S, Se or Te) 2H structure has been found as the most stable except for WTe_2[14].

Their layered structure weakly bonded by vdW forces facilitates the fabrication of TMDs nanosheets by reducing the number of layers via exfoliation. For thicknesses of 10 nm or less TMDs experience the quantum confinement effect, which is the change and even enhancement of electronic, optical structural and mechanical properties when the material is reduced to this smaller size[17-19]. Some of the changes experienced can be increased bandgap[20], indirect to direct bandgap transition[21], semi metallic to semiconductor behavior[22] or improved catalytic activity[23]. For that reason, 2D TMDs with 2H layered structure as MoS_2, $MoSe_2$, WSe_2 and WS_2 stand out due to their semiconductor nature, narrow and tunable bandgap (around 1-2eV) and high light absorption coefficients (10^5 – 10^6 cm^{-1})[24].

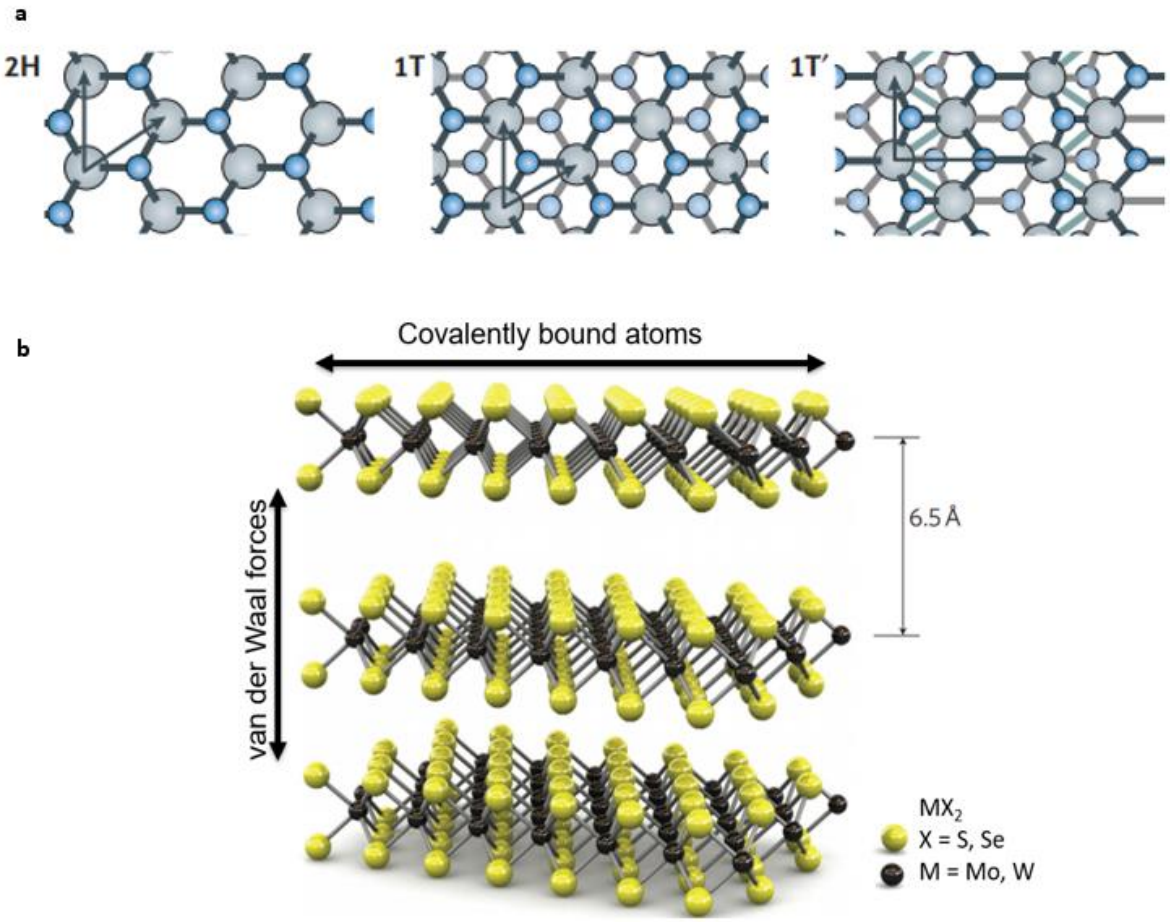

Figure 1. (a) Common structural phases of TMDs[14]. (b) Atomic structure of TMDs in 2H semiconducting form. Figure adapted from Liu et al.

Furthermore, among the mentioned semiconducting TMDs different properties and behaviour are found depending on the combination of atoms. For instance, the electronic bandgap is different for each TMD (Figure 2a), making them more suitable for hydrogen evolution reaction (HER) or oxygen evolution reaction (OER) depending on the proximity of their bandgaps to redox potentials of these reactions. For instance, MoS_2 experiences changes in its bandgap depending on the number of layers, as it goes from 1.29 eV (indirect) in bulk material to 1.9eV (direct) at a monolayer thickness[25,26,27]. The tunability of the bandgap is an interesting property as it can allow the same material to take part in different applications where specific bandgap requirements are needed.

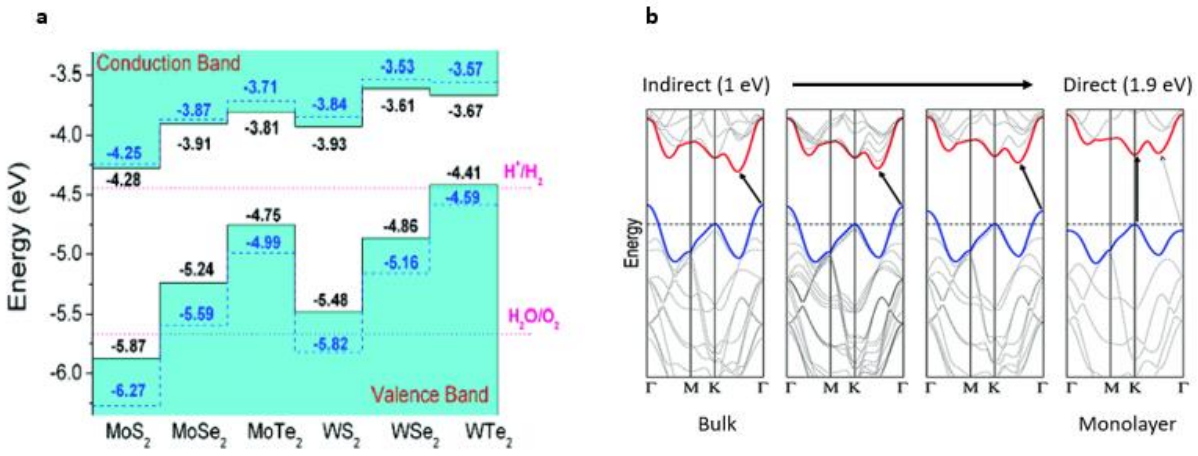

Figure 2 (a) Overview of G6-TMDs bandgaps[33]. (b) MoS_2 bandgap dependance on number of layers[19].

Indeed, both MoS_2 and WSe_2 have been a focus of research in recent years due to their optoelectronic properties, photoelectrochemical performance and strong absorption in the visible range[28].

First of all, MoS_2 is robust, earth abundant and naturally shows a strong n-type behavior. Besides, MoS_2 also stands out for its strong photoluminescence and environmental stability[29].

On the other hand, WSe_2 is unique for its intrinsic p-type behavior, high absorption coefficient and strong photoluminescence[30]. Furthermore, the WSe_2 bandgap is suitable for the water reduction reaction[31] (Figure 2a) and is therefore a good candidate to act as a photocathode for photoelectrochemical water splitting. Indeed, Lewis et al. followed this approach and obtained a >7% efficiency for HER by using in acidic conditions a single WSe_2 crystal coated with a Pt-Ru catalyst[32].

Finally, another popular TMD is WS_2, which naturally shows a n-type behavior[33] and exhibits a sizable bandgap as well as good optoelectronic properties[34,35]. Indeed, its high emission quantum yield and large exciton/trion binding energy among other interesting features make WS_2 promising candidate for next-generation nanoelectronics and optoelectronics[36].

For the above-mentioned reasons, MoS_2, WSe_2 and WS_2 were chosen as exemplorary materials for this examining doping in 2D TMDs.

1.2 Obtaining 2D TMDs

As previously mentioned, TMDs should be thinned to a 2D dimensions to take advantage of their unique optoelectronic properties that arise a result of quantum confinement. Therefore, several methods have been developed for this purpose. Among them, mechanical exfoliation, chemical vapor deposition (CVD) and solution-phase methods have been widely used in recent years[37].

Mechanical exfoliation and CVD allow the obtention of high quality 2D TMDs but strict temperature and vacuum requirements as well as direct deposition of the nanosheets into the substrates are the main drawbacks for these methods to be applied at large scale[38]. Therefore, solution-phase methods like liquid-assisted exfoliation, chemical and electrochemical intercalation stand out because of their scalability and low cost[39,40].

In liquid-assisted exfoliation, a layered TMD crystal is paired with a solvent which should have a surface energy close to that of the TMD basal plane. Then, due to the interaction between the solvent molecules and the surface of the layered material the TMD can be exfoliated by means of an ultrasonication (Figure 3). This exfoliation method leads to a flake dispersion and maintains the 2H crystal structure and therefore the semiconducting properties of the material[41]. However, the obtained nanoflakes are likely to present defects as a result to the harsh nature of ultrasonication. This has a negative effect on the TMDs' optoelectronic properties and performance[42].

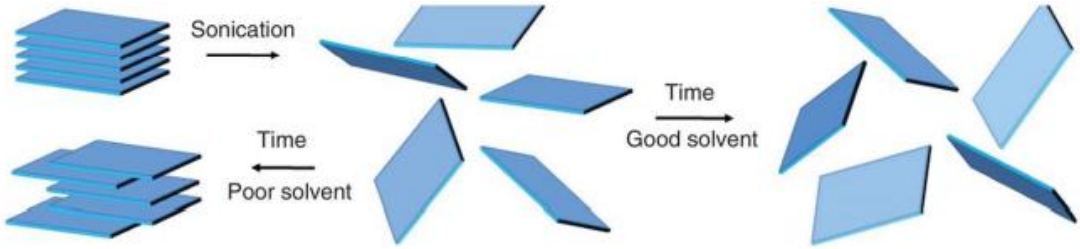

Figure 3. Solvent-assisted exfoliation[42]

On the other hand, chemical intercalation (Figure 4a) introduces little alkali metal ions such as Li^+ or Na^+ between the TMD layers and agitation or sonication is applied afterwards in order to separate them. However, the main drawback of this method is the transition of the TMD structure from the semiconducting 2H phase to the semi metallic 1T phase (Figure 4c) due to electron injection into MoS_2 crystals by the intercalation of Li^+ atoms[43]. The 2H phase can be recovered but this requires an additional step of high temperature annealing of high-powered lasers, limiting scalability[44].

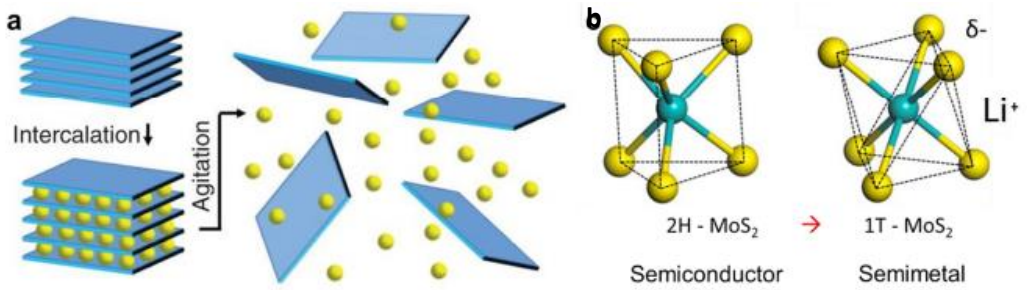

Figure 4a. Chemical intercalation and exfoliation. Figure 4b. Phase transition to 2H to 1T in MoS_2 after chemical intercalation and exfoliation. Nicolosi et al. Science, 2013

Conversely, a method that follows a similar principle as chemical intercalation but avoids the mentioned phase transition from 2H to 1T can be found in electrochemical intercalation of large cations. Here, non-metallic species namely quaternary ammonium molecules (e.g. THAB) are electrochemically intercalated between a single crystal TMD layers and a sonication is applied afterwards to separate these layers (Figure 5). The big size of THAB (d ≈ 20 Å in contrast to d ≈ 2 Å of Li^+ atoms) limits the number of intercalated molecules and as the process is electrochemically controlled the number of electrons injected into the TMD crystal is limited, avoiding undesired phase transitions[45].

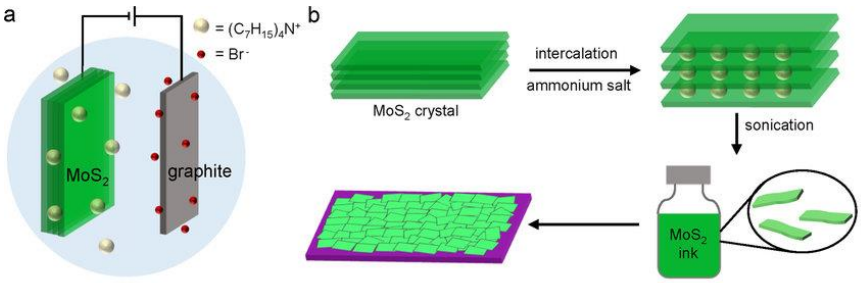

Figure 5. (a) THA^+ electrochemical intercalation setup[46] (b) THA^+ intercalation and exfoliation process scheme.

Indeed, Lin, Z. et al[46] show that MoS_2 nanosheets exfoliated by THA^+ intercalation were found to be larger, thinner and with less defects compared to those exfoliated by Li^+ intercalation. They also show strong photoluminescence and semiconducting behavior (Figure 6d), light absorption at the visible range (Figure 6b) and promising performance as a field effect transistor (Figure 6e) unlike Li^+ intercalated MoS_2 nanosheets.

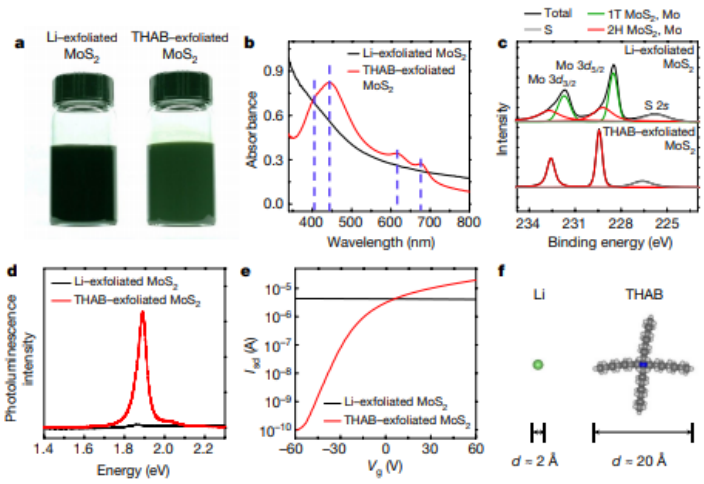

Figure 6. (a) Li-exfoliated and THAB-exfoliated MoS_2 vs Li^+ intercalation nanosheets solutions. (b) UV-VIS spectroscopy analysis of exfoliated nanosheets. (c) RAMAN spectroscopy analysis of exfoliated nanosheets. (d) Photoluminescence spectroscopy analysis of exfoliated nanosheets. (e) Transfer curves of FET generated with MoS_2 Li and THAB exfoliated nanosheets. (f) Size of Li and THAB molecules[46]

However, the main drawback of electrochemical intercalation of modules is that a single TMD crystal is needed as an initial material, so the process becomes expensive and limits its scalability.

Therefore, in order to make this method scalable an approach consisting of an electrochemical intercalation of modules starting from a TMD pellet made from commercial powder instead of a TMD single crystal has been developed by EPFL's LIMNO research group. However, as crystal growth is needed at pellet's surface to allow THA^+ intercalation, an annealing process has to be applied to the pellet before starting with intercalation. Moreover, this annealing process helps to terminate chalcogen vacancies of TMDs and other impurities present in the material[47]. As expected, vertical crystal growth is reached at pellet's surface after 48h of annealing (Figure 7). This annealing step improves the conductivity of the pellet by providing electron percolation pathways, crucial for electrochemical intercalation.

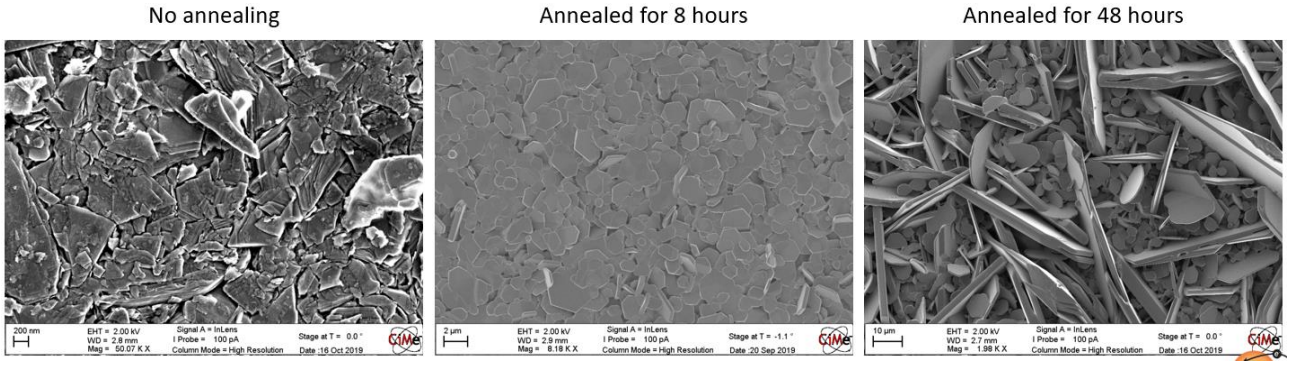

Figure 7. Effect of annealing process in TMD pellet crystal growth

Indeed, MoS_2 nanosheets obtained using THA^+ intercalation and exfoliation from a pellet exhibit larger and thinner flakes compared to MoS_2 nanosheets obtained by solvent-assisted exfoliation, confirmed by size analysis (Figure 8a) and UV-VIS spectroscopy analysis (Figure 8b). Therefore, they show improved optoelectronic properties such as higher photoluminescence (Figure 8c) and higher photocurrent (Figure 8d).

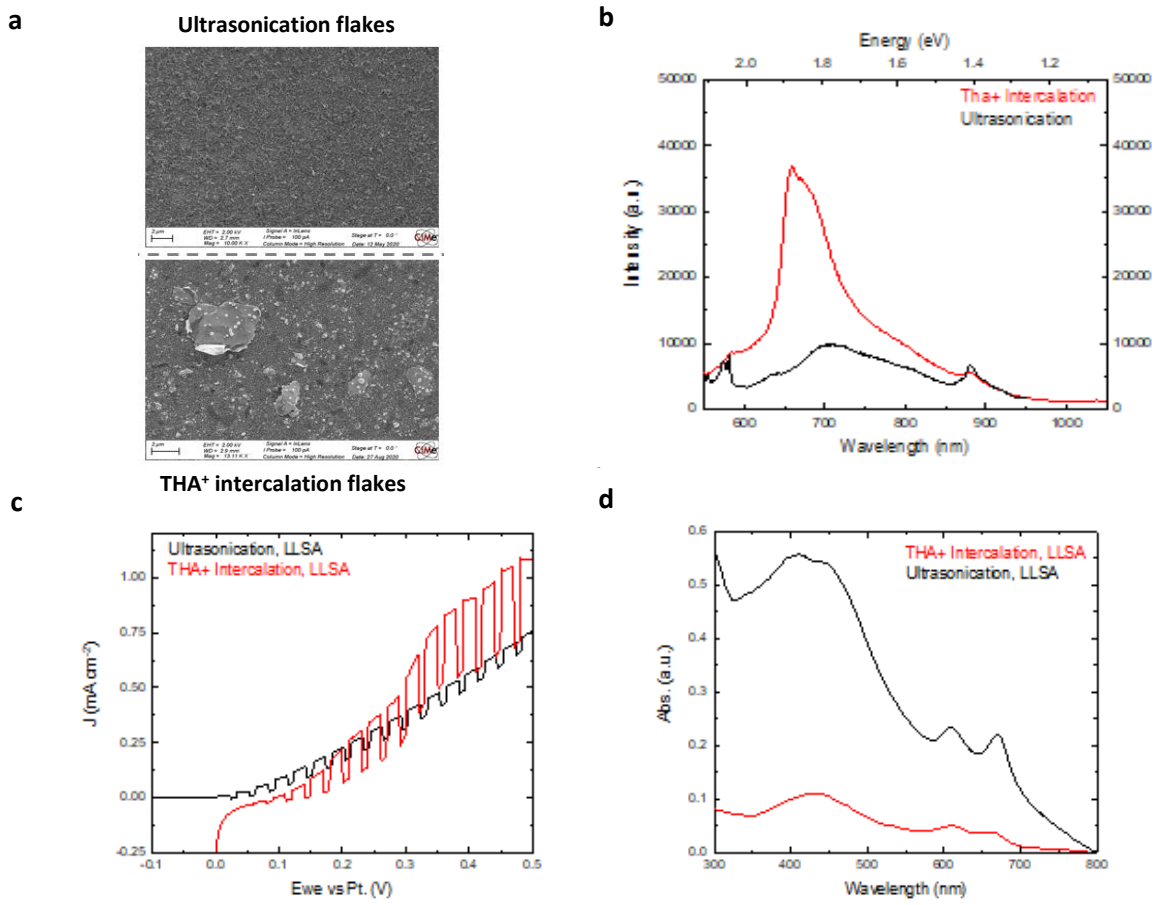

Figure 8. (a) SEM images of ultrasonicated and THA+ intercalated MoS_2 films. (b) PL spectroscopy analysis. (c) Photoelectrochemical performance analysis. (d) UV-VIS spectroscopy analysis

1.3 Doping in TMDs

As seen in Sections 1.1. and 1.2. bandgaps of TMDs can be tuned depending on several factors including their composition, number of layers or flake size, enabling them to take part in a wide range of applications. Moreover, in semiconducting TMDs the structural, physical, chemical and optoelectronic properties can also be easily modified by doping with, for instance, metallic atoms[48]. This allows to additional fine tuning of optoelectronic properties and further expands the range of possible applications[49-65].

Indeed, the most common doping strategy is substitutional doping with transition metal elements, as it has been demonstrated to be suitable for changing the material properties and behavior[26]. As shown in Figure 9, the dopant element (represented by a blue sphere) occupies the place of the metal (black sphere) in the TMD structure.

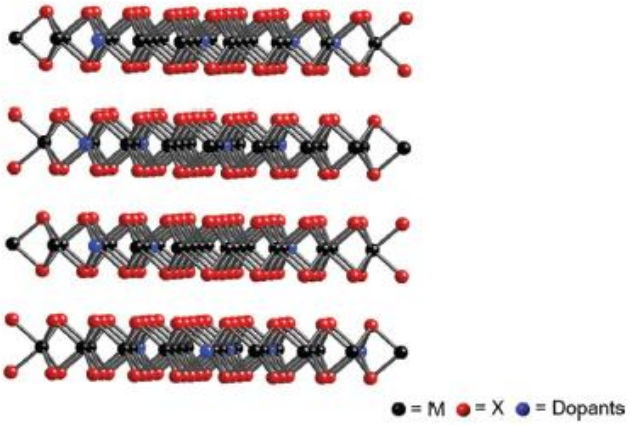

Figure 9. Substitutional doping in TMDs[47]

This process is favored because the electronic structure of both atoms is similar. Indeed, Molybdenum (Mo) has a $4d^5$ $5s^1$ structure in the last orbital, Tungsten (W) has $6s^2$ $4f^{14}$ $5d^4$ while Niobium's (Nb) last orbital structure is $4d^4$ $5s^1$, so that the occupation in d-orbital is similar (Figure 10). Furthermore, lattice structures of MoS_2 and NbS_2 present 2H configuration and their lattice parameters are also similar ([a, b, c] = [3.16, 3.16, 12.29] for MoS_2 and [3.32, 3.32, 11.94] for NbS_2)[26]. Therefore, Nb has been demonstrated to be a suitable p-type substitutional dopant for either n-type TMDs (as MoS_2 or WS_2) or p-type ones (as WSe_2) among other transition metals[26].

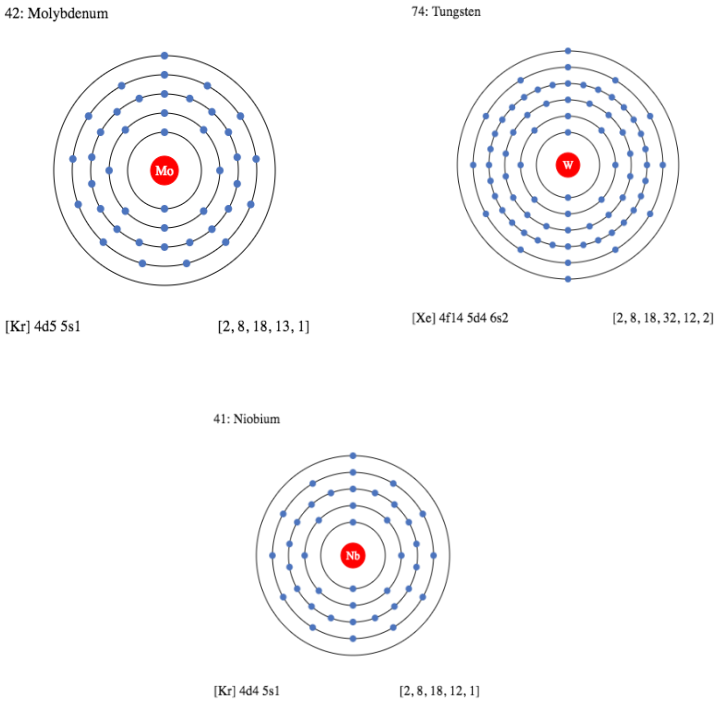

Figure 10. Electronic structure of Mo, W and Nb
https://www.schoolmykids.com/learn/interactive-periodic-table/mo-molybdenum

In recent years, several approaches about doping in TMDs have been developed depending on which properties want to be modified or which behavior wants to be achieved in the material.

For instance, the incorporation of a p-type dopant (which gives excess holes) to a n-type TMD MoS_2 has been demonstrated to give the material an ambipolar (p-type and n-type) behavior. For instance, Mengge Li et al. obtained an ambipolar behavior for Nb-doped MoS_2[49], p-type behavior after Nb doping of MoS_2 was also confirmed by Masihhur R. et al.[50] getting a high hole concentration of 3.1×10^{20} cm^{-3} and a high hole mobility of 8.5 $cm^2/V{\cdot}s$. Consequently, Nb-doped MoS_2 has been used as a building block of ambipolar transistors[51,52].

Indeed, p-type dopants can also be incorporated to p-type TMDs as WSe_2 to modify and enhance its optoelectronic properties such as bandgap width, photoresponsivity[53] or charge carrier transport[54], which are key factors in photoelectrochemical devices. Therefore, Nb-doping has been shown to enhance the performance of WSe_2 compared to the undoped material in FETs[55,56]. This has potential advantages for optical devices like photodetectors due to enhanced photoresponsivity.

Following the same idea, the addition of n-type dopants to n-type TMDs is an interesting approach to enhance intrinsic behaviors. In a theoretical study by Dolui et al.[57] Rhenium (Re) was suggested to be the most appropriate n-type dopant for MoS_2 among other n-type transition metals. Furthermore, several experimental reports [58,59,60] showed the feasibility of Re incorporation to MoS_2 via physical vapor transport.

However, nowadays the number of reports which study Re-doped MoS_2 optoelectronic properties and feasible applications is still limited. Among them, L. Yuanyuan et al. found a decay of photocarrier lifetime when doping the material, which could be useful for high-speed emitters or detectors[61] and Re doping has been proven to enhance catalytic activity of 1T phase MoS_2[62].

Also, Zn dopants have been included successfully to MoS_2 in order to improve its photoresponsivity in optoelectronic devices as photodetectors[63,64] or to enhance MoS_2 catalytic activity for HER[65].

Additionally, we note that physical vapor transport methods experience the same limitations as previously stated. Thus, in order to envision large scale fabrication of devices using doped 2D materials, a scalable approach must be developed.

1.4 Objectives and scope of the project

According to the introductory section, doping TMDs to tune and improve its optoelectronic properties can potentially make these materials even more promising. However, it is still not clear what is the effect of the different dopant atoms concentrations in the TMD on its optoelectronic properties and crystal structure, as the dopant atomic percentages in published reports are variable[49-65].

Thus, having the knowledge about how TMD properties evolve as a function of dopant concentrations would be useful to optimize the material depending on the desired properties. Considering the interest aroused by this TMD in recent years (Section 1.1.), the analysis will be mainly focused on MoS_2 with Nb-doping because of their mutual suitability (Section 1.3.).

Moreover, as commented in Section 1.2. 2D TMDs will be obtained by electrochemical intercalation with THA^+ but starting from a pellet made from commercial TMD powder instead of a single TMD crystal, which is a unique method developed by LIMNO research group that can make electrochemical intercalation easily scalable. The experiments performed in this project will help to add more evidence about the suitability of this method as well as to determine if it is possible to produce doped TMDs.

More concretely, the first goal of this project will be to characterize and identify Nb-presence in the MoS_2 crystal lattice of the pellets and in the thin films obtained by solution-processable methods.

Then, optoelectronic properties including absorbance, photoluminescence, photocurrent density and charge mobility will be analyzed for a range of dopant concentrations.

Finally, if a change or even an improvement is seen on these properties, the next goal will be to test the doped TMDs in potential applications such as FETs and photoelectrodes in PECs.

In addition, an initial approach about n-type doping in MoS_2 and an overview of Nb doping in other TMDs as WS_2 or WSe_2 will be provided. This serves to support the ability to dope a variety of TMD materials with different dopants, showcasing the adaptability of the pellet-THA^+ intercalation exfoliation method.

Chapter 2 Nb-doped MoS_2 production and characterization

In this Chapter the incorporation of Nb to MoS_2 is studied by characterizing the doped annealed pellets, followed by the exfoliated doped nanoflakes.

First of all, MoS_2 and Nb powders are thoroughly mixed and then pressed at 10kPa using a hydraulic pellet press so that a compact, round disk is formed. Then, the pellets are sealed in quartz tubes with excess S powder and heated to 1100°C for 48h in vacuum to avoid oxidation[66]. The pellets are then intercalated with THA^+ molecules and exfoliated in 1-Methyl-2-pyrrolidone (NMP) by means of a low-power bath sonication. Because of its surface tension of 40 mJm^{-2}, which is close to the surface energy of layered materials[67], NMP has been demonstrated to be the most efficient solvent for TMDs as MoS_2[68]. After centrifugation, nanosheet dispersions are obtained by extracting the supernatant, discarding the precipitate as it contains the remaining undesirable bulk material.

Once the Nb-doped MoS_2 nanoflake solution is ready, these flakes are deposited onto a substrate (FTO) by liquid-liquid interfacial self-assembly (LLISA, see Methods). This film deposition method is continuously scalable and avoids the main drawbacks (i.e. aggregation and precipitation) of other popular solution-based film deposition techniques like spin coating or drop casting, [69,70]. Finally, the films deposited onto the substrates are introduced in a vacuum oven for 2h at 200°C to get rid of possible remaining solvent and increase substrate-nanoflake adhesion. A flowchart of the explained procedure is shown in Figure 11 and extended information about it can be found in Methods.

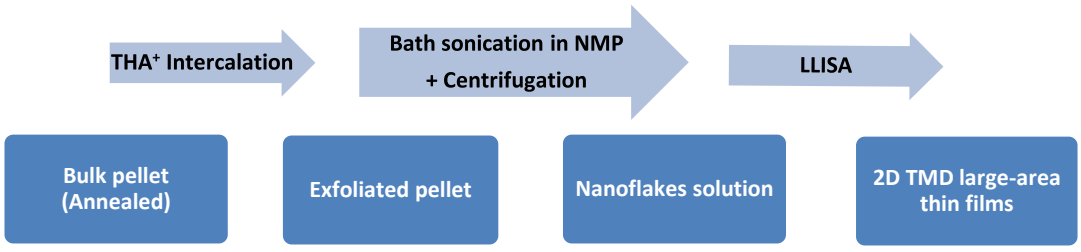

Figure 11. Flowchart of exfoliated TMD pellets and 2D thin films fabrication

Regarding the tested Nb atomic percentages in MoS_2, they have been defined according to what has been done in previous research. For instance, Suh, J. & co. tried 1% and 5% atomic Nb doped MoS_2 for catalysis in hydrogen and oxygen evolution reactions[71]. Besides, lower concentrations as 0.8% have been demonstrated to be sufficient for experimenting changes in the TMD properties and the resulting material can be suitable for FET devices[49]. Thus, a range from 0.25% Nb to 6% Nb atomic ratio respect to Mo has been tested, focusing more on the lower side of the range as high dopant agent concentrations can be harmful to device's optoelectronic properties.

2.1 Nb-doped MoS_2 pellet characterization

First of all, several characterization techniques were used to explore Nb-doped MoS_2 annealed pellets with the aim of identify Nb presence in MoS_2 crystal structure and see how is it modified because of the dopant agent incorporation.

2.1.1 Elemental analysis of Nb-doped MoS_2 pellets (ICP-MS)

An elemental analysis of Nb-doped and undoped MoS_2 pellets by means of inductively coupled plasma mass spectrometry (ICP-MS) is carried out in order to determine Nb presence in these pellets and to have an estimation about the actual Nb atomic percentage respect to Mo atoms.

Figure 12 results show Nb presence in all doped samples and compares the expected Nb atomic percentage with the atomic Nb percentage calculated by ICP-MS, where differences regarding exact concentrations are seen but %Nb increases as desired. In addition, a slight Nb signal corresponding to 0.18% atomic is obtained for the undoped MoS_2 sample, probably due to impurities present in the undoped commercial powder.

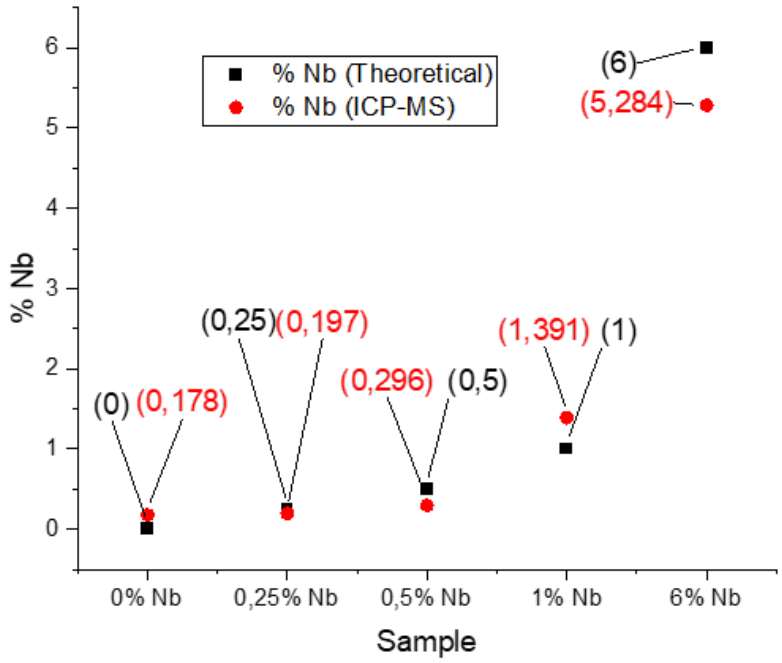

Figure 12. ICP-MS of undoped and Nb-doped MoS_2 powders results

2.1.2 Scanning electron microscopy (SEM) analysis

Scanning electron microscopy analysis was used to visually observe what effect, if any, Nb inclusion in the pellet had on the resulting crystal growth in pellets.

Therefore, undoped and Nb-doped MoS_2 pellets have been analyzed by SEM and the images obtained are presented in Figure 13. Here, the main change between undoped and Nb-doped pellets' surface topography is the crystal growth and growth ratio, that is flat compared to perpendicular growth. While undoped MoS_2 exhibits lots of vertical crystal growth, in Nb-doped samples the crystal growth is noticeably lower in consonance with higher amounts of Nb. Additionally, crystal size from edge to edge also becomes lower when the Nb percentage is higher, and the surface becomes more irregular and fragile from 1% Nb doping. In addition, zooming in on the 6% Nb doped pellet shows a new crystal shape (marked with a green circle) which did not appear in any of the other samples.

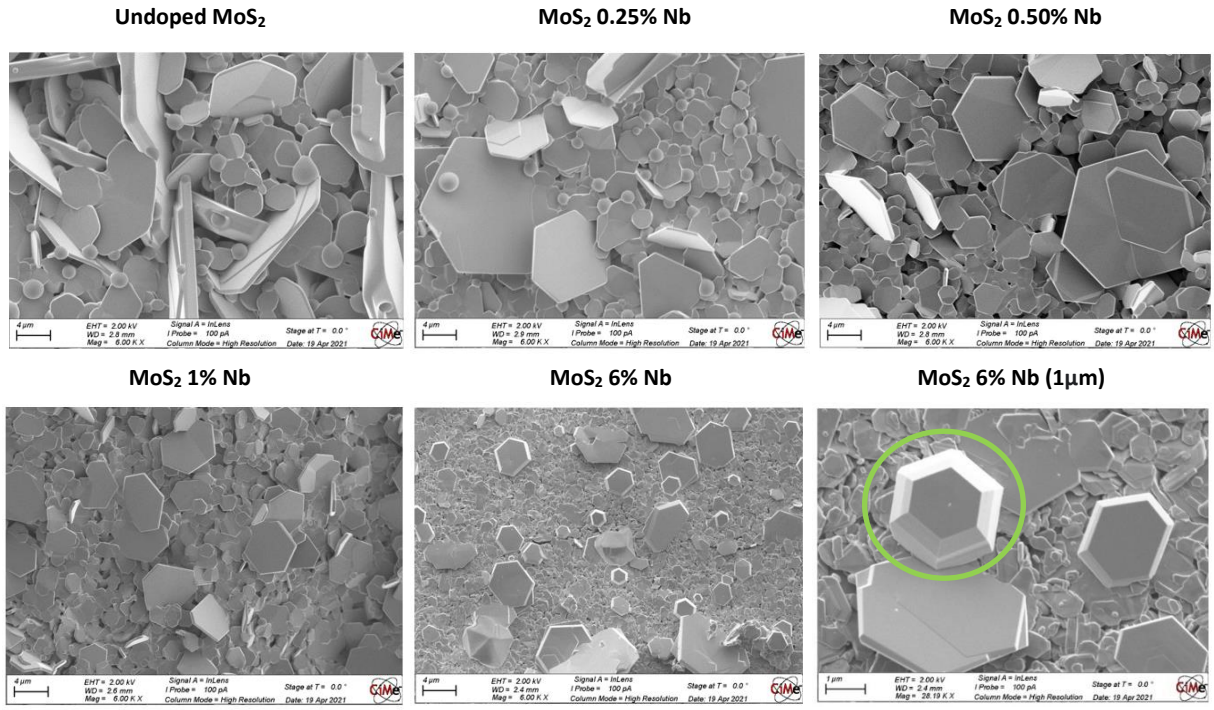

Figure 13. SEM images of undoped and Nb-doped MoS_2 pellets

2.1.3 X-Ray Diffraction (XRD) analysis

SEM analysis suggested that Nb-doping leads to changes in MoS_2 crystal domains and even structure. Thus, it can be expected that the incorporation of Nb atoms was successful and has an effect on the crystal structure of MoS_2. Therefore, lattice parameters and crystallinity of undoped and Nb-doped MoS_2 samples have been analyzed by means of X-Ray Diffraction (XRD).

Fine powders of Nb-doped and undoped MoS_2 were prepared by grinding the pellets and studied using transmission XRD, obtaining the spectra in Figure 14. Here, an intensity decrease and peak widening is seen when Nb concentration is increased. As XRD peaks are more intense and sharper when the sample is more crystalline, this gives a sign that Nb atoms are present in MoS_2 lattice and they are decreasing its crystallinity. Additionally, peak broadening is a sign of smaller crystal domains, supporting observations made in SEM. Differences in peak intensities are also observed, agreeing with the difference in pellet morphology observed in SEM.

Furthermore, some new peaks (marked with red circles) start to be visible in 6% Nb doped sample, which suggests the existence of new crystal shapes as those seen in SEM images.

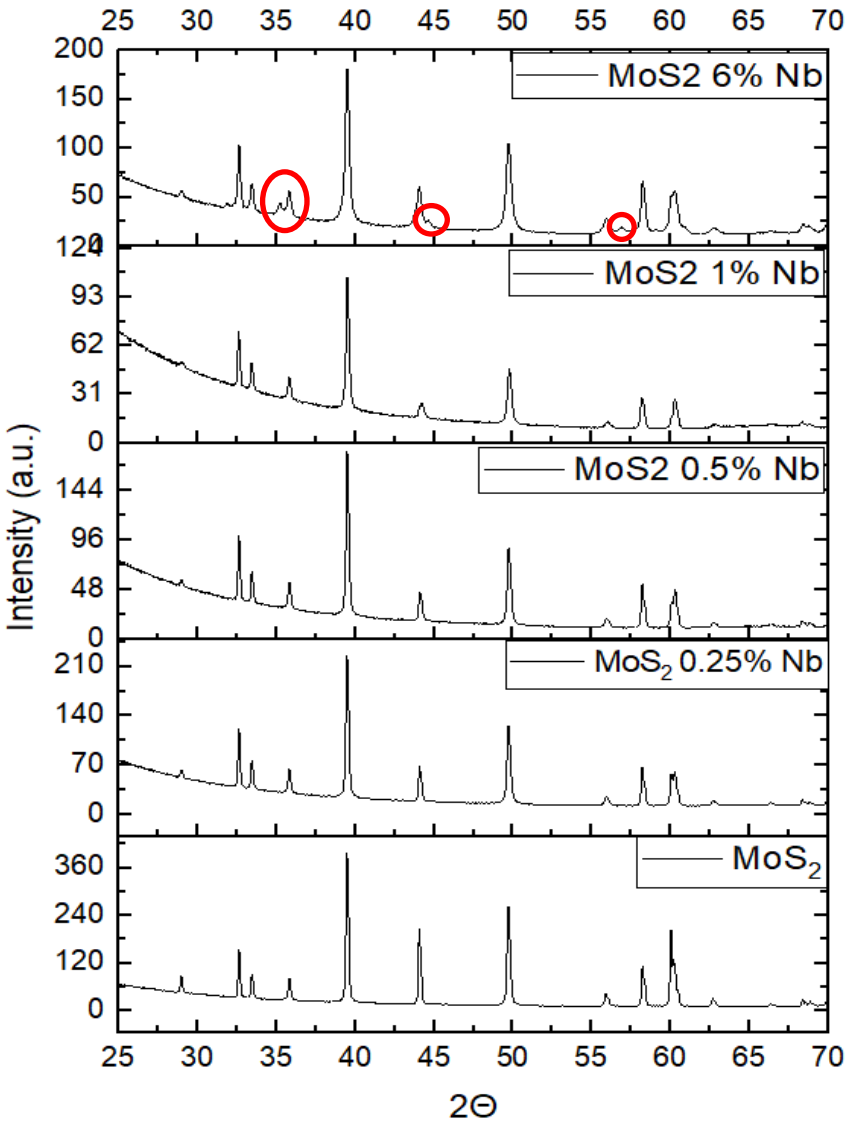

Figure 14. XRD spectrums Nb-doped MoS_2

Furthermore, from the positions identified in XRD, the d-spacings can be calculated according to Brags law, allowing for the calculation of the lattice parameters of MoS_2. Figure 15 shows the evolution of lattice constants a and c as a function of Nb percentage. Changes observed could be caused by different stacking configurations of Nb:MoS_2 and or by the slight difference of size between MoS_2 (a=3.17 Å, c=12.31 Å) and NbS_2 (a=3.32 Å, c=11.97 Å)[72] structures. Initially, lattice parameters decrease as a function of Nb addition probably due to the smaller size of the incorporated Nb atom compared to Mo atom. However, after a certain point lattice parameters increase so that it suggests an expansion of the crystal lattice, possibly related to the larger parameters of NbS_2 which will be more likely to be found with increasing amounts of NbS_2. However, additional data points would be needed to draw more concrete conclusions.

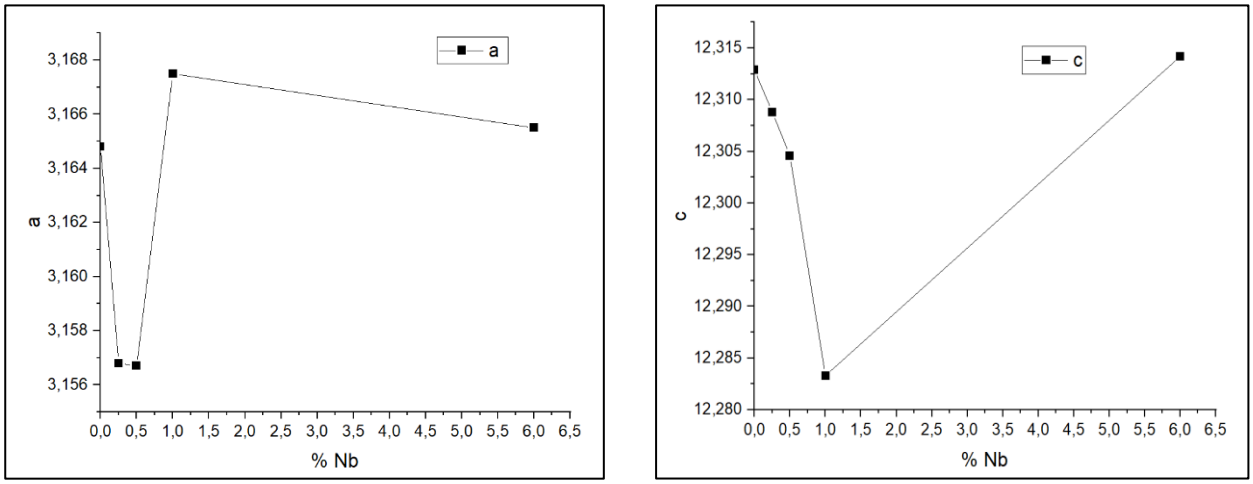

Figure 15. MoS_2 lattice parameters (a and c) evolution with Nb addition

2.1.4 Resistivity and sheet resistance analysis

Reaching the point where it has been proved that Nb is successfully incorporated to MoS_2 crystal lattice and leads to changes on it, changes in material's electronic properties as conductivity or resistivity can be expected. Therefore, edge-to-edge resistivity and sheet resistance of undoped and Nb-doped MoS_2 pellets were measured.

First, MoS_2 has a sheet resistance of 9319 Ω/sq. and a resistivity of 3320 kΩ so it behaves as an insulator. However, even with a small %Nb added both properties experience a decay of around 4 orders of magnitude as seen in 0.25% Nb-doped MoS_2 sheet resistance (1.23 Ω/sq.) and resistivity (0.0424 kΩ). The addition of delocalized charges and impurities on MoS_2 structure due to Nb doping increase the material's conductivity. Moreover, as expected Nb-doped samples become more conductive with higher Nb concentrations even though the change is less noticeable from 0.75% Nb on-wards (Figure 16). This is likely because a %Nb saturation point is reached around this concentration.

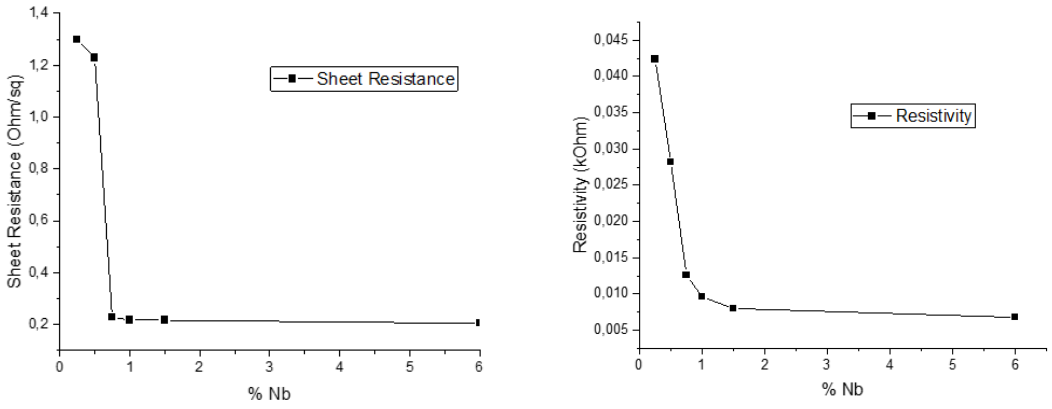

Figure 16. Resistivity and sheet resistance of Nb-doped MoS_2 pellets at different dopant concentrations

2.2 Nb-doped MoS_2 nanoflakes solution and 2D large-area thin films characterization

After proving Nb incorporation to MoS_2 pellets and its effects on the TMD crystal structure and electronic properties, the next step is to check if these changes are maintained when the resulting material is thinned and transferred into 2D large-area thin films by means of exfoliation via THA^+ intercalation followed by LLISA film deposition (Figure 11 and Methods).

First of all, undoped and Nb-doped MoS_2 nanoflakes solutions were analyzed by ICP-MS. Expected and measured values are compared in Figure 17. Though differences are seen, the concentration reliably increases as desired, showing that Nb atoms are indeed present in the final nanoflake dispersions. Notably, possible impurities detected in undoped MoS_2 powder are low enough to be undetectable in undoped films. However, we note that the same is true for the 0.25% Nb-doped sample where the Nb signal is below detection limit.

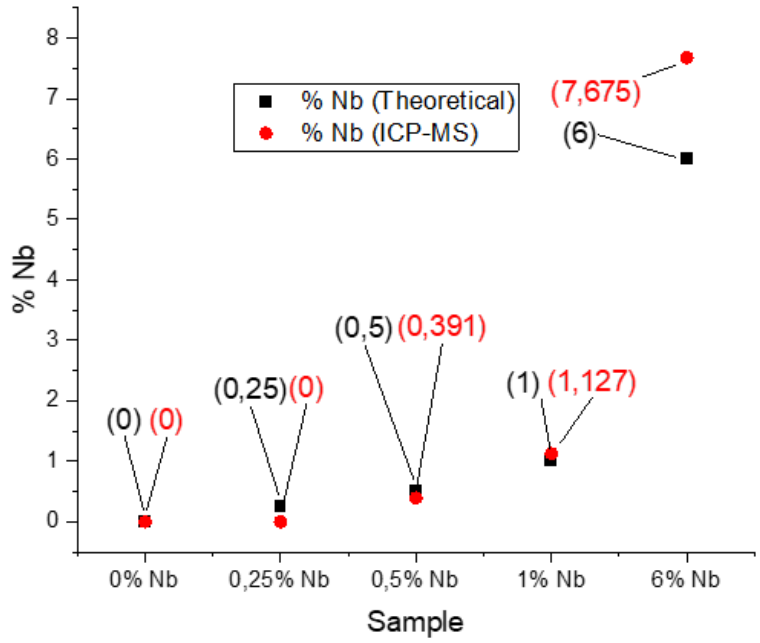

Figure 17. Expected %Nb and ICP-MS measured %Nb in Nb-doped MoS_2 flakes

Then, undoped and Nb-doped MoS_2 nanoflakes solutions were characterized by Zeta Potential analysis. To do this measurement, 2µl of each solution were diluted in 20ml of miliQ water and introduced into the instrument's measuring chamber. The results obtained are shown and Figure 18, where all samples have negative values of zeta potential as they are negatively charged due to sulfur atoms in MoS_2. Initially, Nb doping up to 0.75% Nb makes zeta potential less negative by reducing the intrinsic n-type behavior of MoS_2. However, from 0.5% Nb to 1% Nb the zeta potential

magnitude starts to increase probably because of the high concentration of defects in MoS_2. This leads to higher stability of the colloidal system as the particles have more surface charges and therefore higher magnitude of zeta potential.

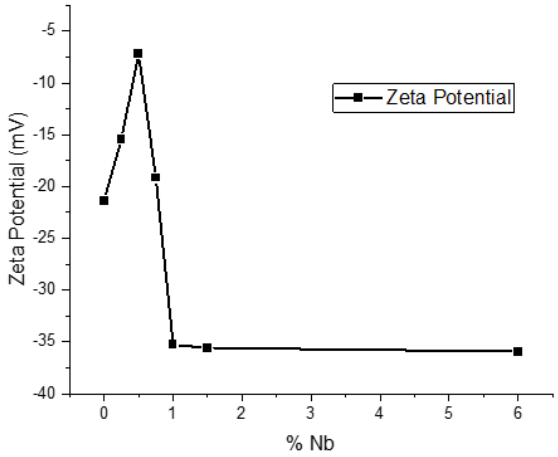

Figure 18. Zeta potential evolution of Nb-doped MoS_2 nanoflakes solutions

The previous characterization of the nanoflake dispersions suggest that Nb atoms are still present in MoS_2 nanoflakes after exfoliation, so the next step is to characterize thin films made from these solutions by LLISA film deposition method.

First of all, as Raman spectroscopy gives a unique spectrum for each different sample composition this characterization technique has been used to analyze undoped MoS_2 and Nb-doped MoS_2 films.

Looking at Figure 19, undoped MoS_2 shows two clear peaks at 379 cm^{-1} and 405 cm^{-1}. Once the percentage of Nb increases a progressive right shifting of the main peaks occurs. This behavior is also observed in literature[49] an occurs as a result of distortion experienced in MoS_2 crystal lattice when Nb is added, which lead to different vibration modes for doped and undoped samples.

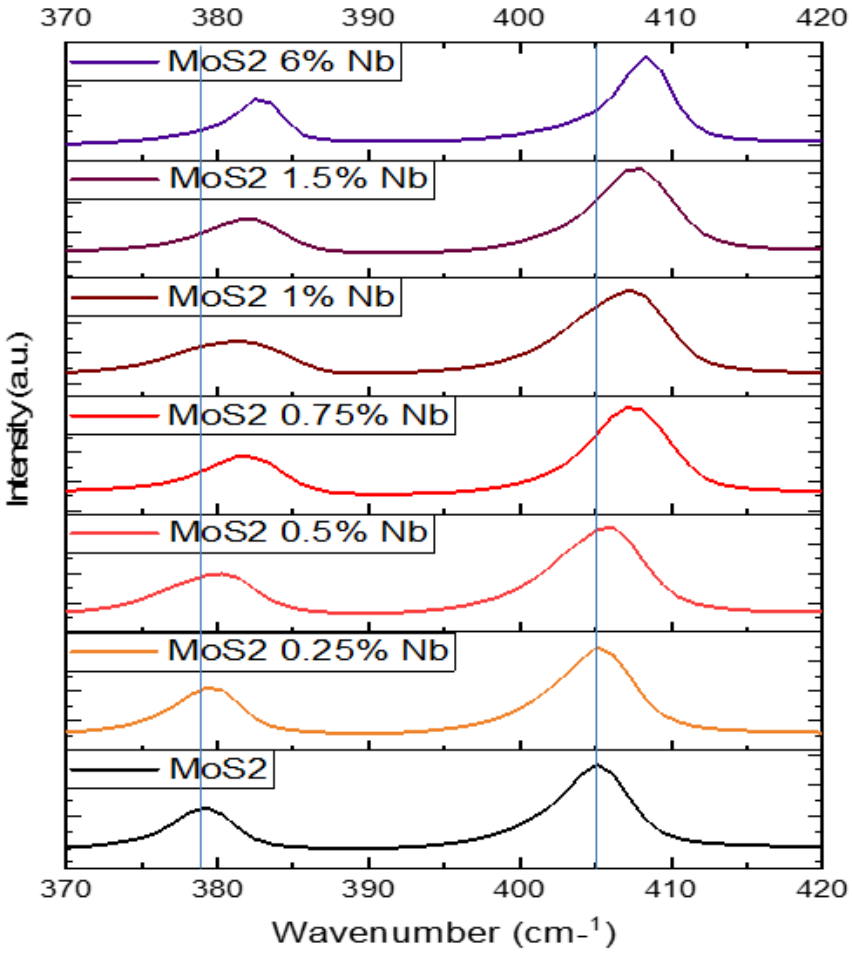

Figure 19. RAMAN spectra of undoped and Nb-doped MoS_2 films

Besides, qualitative nanoflakes analysis was carried out using SEM images from the generated films (Figure 20). Here, it can be observed that the flakes become smaller and thicker when Nb concentration is higher. Probably, the yield of THA^+ intercalation molecules decreases with Nb-doped MoS_2 pellets as their surface do not contain as much vertical crystal growth as undoped MoS_2 so THA^+ molecules are less likely to be intercalated. Consequently, the exfoliation of Nb-doped MoS_2 will be also worse, leading to thicker flakes. Lastly, smaller starting crystal domains in the pellet lead to nanoflakes with smaller lateral dimensions.

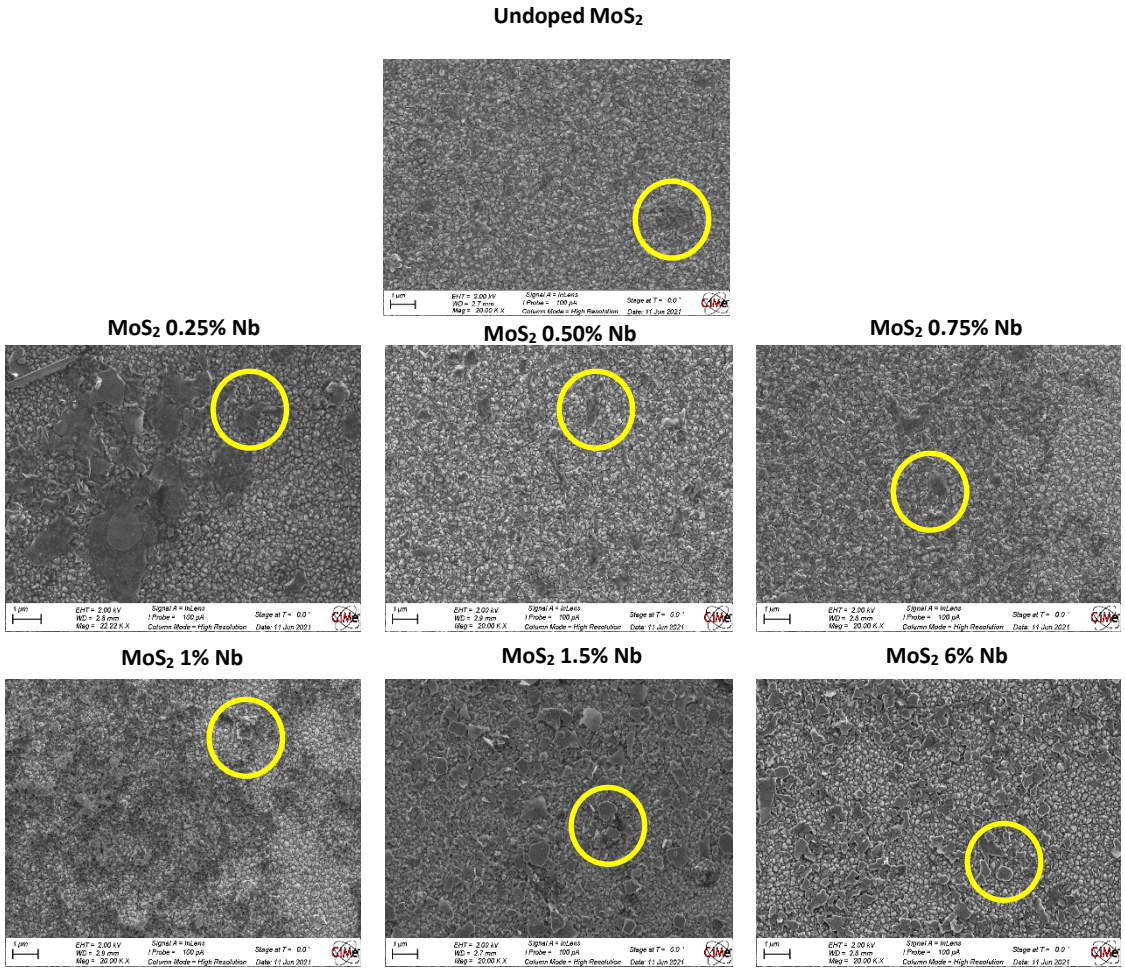

Figure 20. SEM images of undoped and Nb-doped MoS_2 nanoflakes

Finally, the films are also characterized by UV-Vis spectroscopy as it gives information about sample composition, thickness and also it can give qualitative information about the semiconductor's bandgaps.

In Figure 21, as expected in literature[49], the spectrum for the undoped MoS_2 shows the main absorption peak at 664 nm. Then, doping the material leads to a progressive red shifting of this absorption peak up to 675 nm in 6% Nb doped sample, which means a smaller bandgap of Nb-doped MoS_2 compared to undoped. Besides, after normalizing absorbances of all spectrums it is seen that Nb doping (specially at higher concentrations) leads to thicker flakes as the doped samples absorb more light; thicker flakes possess smaller bandgaps as discussed in the introduction section. Finally, as Nb concentration increases there is a red shifting in the absorption peak around 400nm which implies that the lateral dimension of the flakes becomes smaller when MoS_2 is doped. This is supported by the previous SEM images showing smaller dimensions on average as doping increases.

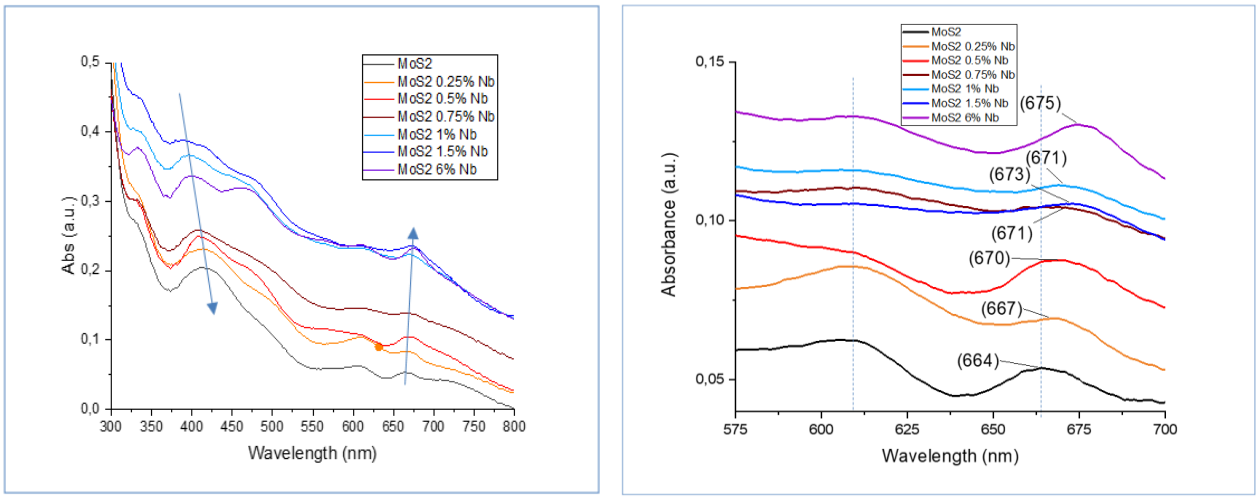

Figure 21. UV-VIS spectroscopy of undoped and Nb-doped MoS_2 films

In summary, ICP-MS confirms that Nb atoms are present in MoS_2 pellets while SEM images show the effects of Nb on MoS_2 crystal domains and growth ratio and XRD analysis gives evidence about MoS_2's crystal structure distortion due to Nb incorporation. Therefore, we conclude that Nb-doping in MoS_2 pellets has been successfully achieved and as a result they show improved conductivity as a function of %Nb.

Moreover, the analysis of the nanoflakes solution made from these exfoliated pellets using electrochemical THA^+ intercalation method gives evidence about Nb presence in the nanoflakes, confirmed by ICP-MS and by changes in the zeta potential of the solution. Finally, shiftings in Raman and UV-Vis spectroscopies from undoped to Nb-doped MoS_2 2D large-area thin films also suggest that Nb atoms are present on them.

Chapter 3 Nb-doped MoS_2 optoelectronic properties and potential applications

As characterization techniques clearly show the presence of Nb atoms in MoS_2 structure both in pellets and films, it is likely to have an effect in the material's optoelectronic properties. Therefore, Nb-doped and undoped MoS_2 films opto-electronic properties have been evaluated along different Nb concentrations.

3.1 Photoluminescence spectroscopy analysis

First of all, photoluminescence (PL) of each sample has been analyzed by means of PL spectroscopy. In Figure 22, PL spectrums of undoped MoS_2 and Nb doped samples are represented. A sharp peak at 668 nm is observed for undoped MoS_2, which indicates strong photoluminescence. Then, photoluminescence is maintained from 0.25% Nb to 0.75% Nb even though PL intensity diminishes. Indeed, for these samples a red shifting in the main PL peak is observed, which means a shrinking of the bandgap, consistent with UV-VIS results. However, increasing Nb atomic concentration more than 0.75% is detrimental to the photoluminescence, as from 1% Nb onwards the materials do not show a clear PL peak and experience a loss in PL intensity. The reason of this decay could be the recombination of the excited charges faster than they can be detected. In this case the Nb sites act as recombination centers, therefore as Nb concentration increases, recombination increases and PL decreases.

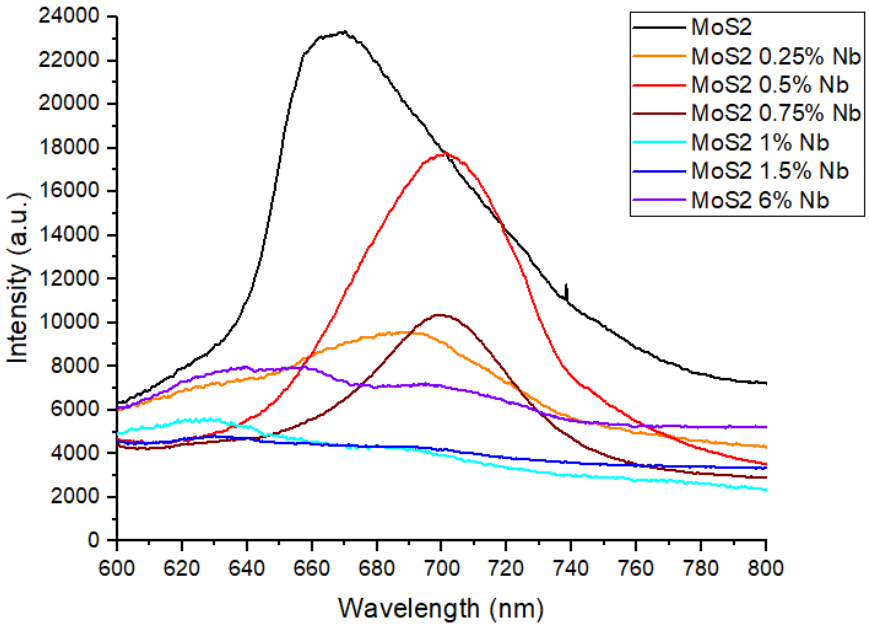

Figure 22. PL spectra of Nb-doped MoS_2 films

3.2 Photoresponsivity and charge carrier analysis (PEC tests)

The photoresponsivity and carrier transport of, for instance, TMDs can be measured by means of testing the material as a photoelectrode in a photoelectrochemical (PEC) cell at a laboratory scale. According to the scheme in Figure 23, the TMD-based photoelectrode harvests incident light (in this case from a Xe lamp) and creates excited electrons which enter into an electric field generated on the TMD-electrolyte solution interface, being attracted or repelled depending on their sign and producing a directional current flow through the cell. Applying a bias modifies this electric field within the material to help of hinder the flow of charges. Then, this electrical energy enables the oxidation or reduction reaction of the electroactive specie to take part at the TMD-based photoelectrode's surface[73,74].

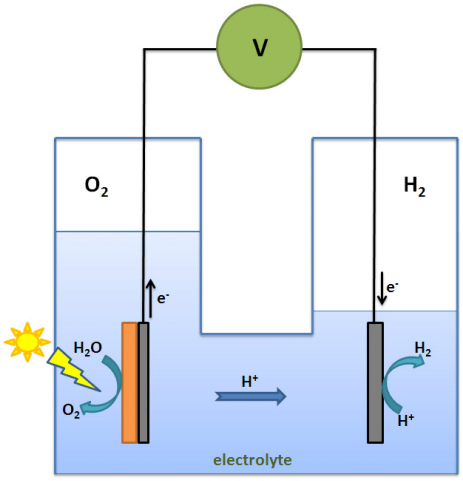

Figure 23. Scheme of a PEC cell. *Catalysts 2*(4), 490-516 (2012)

Therefore, undoped and Nb-doped MoS_2 thin films have been tested as a photoelectrode in non-aqueous (50mM LiI and 25mM TBAFP in Acetonitrile) and aqueous (H_2SO_4 1M) electrolytes. Here, LiI is used to show the n-type behavior of the photoelectrode's material while H_2SO_4 is used to show its p-type behavior.

Linear sweep voltammetry (LSVs) has been applied, which records the current evolution at the working electrode when voltage is applied and therefore gives information about the photoactivity of the working electrode when chopped light is applied.

Additionally, another test applied to examine the photoactivity of a material is an open circuit voltammetry (OCV). In the cell, no current flows and the voltage measured is the voltage necessary to prevent this current flow when the working electrode is in contact with the electrolyte. When light is shined on a photoactive material photogenerated charges are formed and will try to flow. Thus, the difference in voltage measured in the dark and under illumination, also referred to as photovoltage, can therefore be correlated to a material's ability to generate and separate charges.

Figure 24a shows LSV results in non-aqueous conditions, from 0 to 0.6V with light chopping (2 seconds ON, 1 second OFF), where MoS_2 performs the iodide to triiodide oxidation reaction. Here, undoped MoS_2 shows strong photoactivity and charge carrier at positive voltages, which is due to its strong intrinsic n-type behavior. However, Nb-doping of MoS_2 is not beneficial for its photoactivity at non-aqueous conditions (Figure 24b), probably because Nb addition is progressively turning the material to a p-type behavior specially from 0.75% Nb onwards. Furthermore, an increase in dark current (Figure 24c) is seen among doped samples when %Nb is higher. The reason of this trend could be an increase in number of catalytically active sites in MoS_2 structure when more Nb is added, also confirmed by several published studies[75,76] where doping MoS_2 at high concentrations such as 10% improves its catalytical activity for HER due to increased defect concentration. Moreover, in Figure 24d thanks to the OCVs applied it is seen that all doped samples keep the n-type behavior of undoped MoS_2 at non-aqueous conditions and 0.25% and 0.5% Nb slightly enhance MoS_2 ability to separate charges as the photo potential increases for these samples compared to the undoped TMD. However, aligned with the decay in photoactivity, from 0.75% Nb onwards MoS_2 practically loses the capacity to separate charges when light is applied.

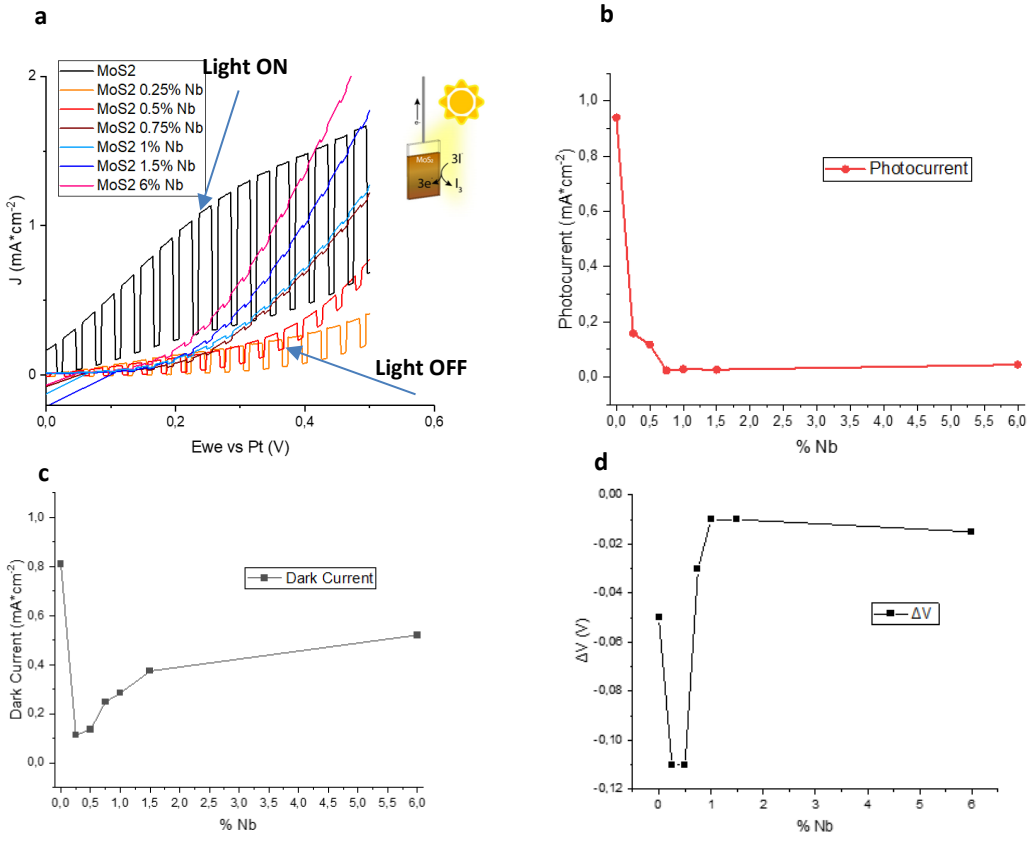

Figure 24. (a) LSV of undoped and Nb-doped MoS_2 films in non-aqueous solution. (b) Photocurrent evolution during LSV along %Nb. (c) Dark current evolution along %Nb during LSV. (d) Potential change evolution during OCP along %Nb.

Furthermore, Figure 25a shows LSV results from -0.5V to 0V with light chopping (2 seconds ON, 1 second OFF) in aqueous conditions suitable for HER reaction. Here, undoped MoS_2 is not able to perform HER evolution in these conditions due

to its strong n-type behavior. 0.25% and 0.5% Nb are not enough to give the material a p-type behavior and therefore perform in aqueous conditions. However, from 0.75% Nb MoS_2 films start to show photoactivity under reductive conditions which is a sign that from this Nb atomic percentage MoS_2 can also exhibit p-type behaviour. Indeed, as seen in Figure 25b the best results regarding photocurrent are found with 1% Nb doped sample and above this concentration photoactivity decays as well as dark current increases (Figure 25c), turning into a more catalytic behaviour. Actually, this change from n-type to p-type behaviour at 0.75% Nb is confirmed by OCV results (Figure 25d), as from this concentration the voltage change when light is applied turns from negative (oxidative, n-type) to positive (reductive, p-type).

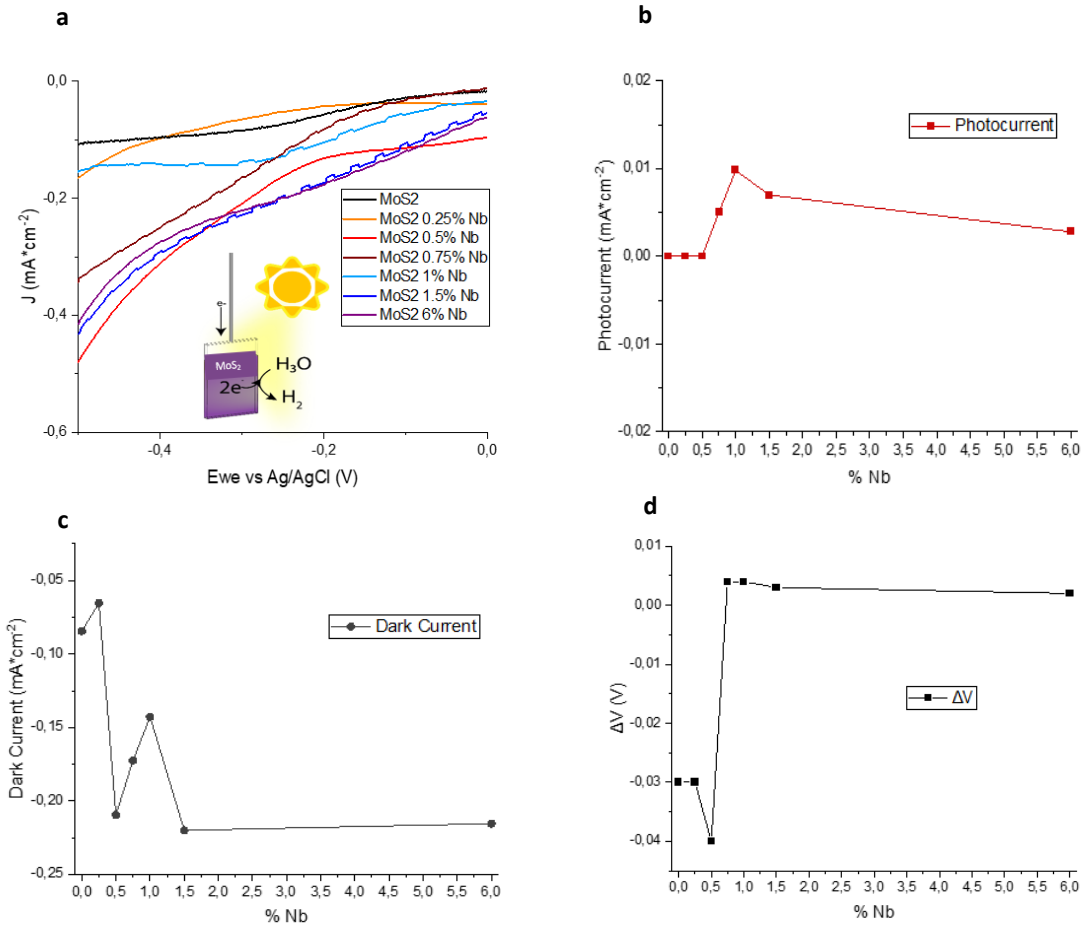

Figure 25. (a) LSV of undoped and Nb-doped MoS_2 films in aqueous solution. (b) Photocurrent evolution during LSV along %Nb. (c) Dark current evolution along %Nb during LSV. (d) Potential change evolution during OCP along %Nb.

Finally, to ensure that the differences seen between undoped and doped MoS_2 in PEC performance can be only attributed to Nb effects and not to different flake sizes effects, an OCV has been carried out with undoped MoS_2 films which nanoflakes solutions' centrifugation process was done at 1000 and 11000 rpm (lower centrifugation speeds lead to bigger flake size). As seen in Supplementary Information (Figure 1), no significant changes are seen between different flake size films' performances.

3.3 Nb-doped MoS_2 applications: Field Effect Transistors (FETs)

As previously mentioned, TMDs like MoS_2 can be used to make thin and high-performance n-type FETs, as several reports have reached high field effect mobility and on/off ratio in MoS_2-based n-type FETs manufactured using solution processable methods[51,77,78,79]. Furthermore, MoS_2 can also perform as an ambipolar (n-type and p-type) FET and Nb-doping can be a way to enhance hole mobility in ambipolar FETs[52].

Thus, we synthetized undoped and Nb-doped MoS_2-based FETs using the solution phase methods described in Figure 11, using gold patterned silicon-SiO2 substrates.

First of all, output and transfer curves of an undoped MoS_2 based n-type FET (Figure 26) confirm the n-type FET behavior of the device and enable the calculation of electron mobility respectively. An electron mobility of 0.08102 $cm^2/(V \cdot s)$ is obtained for these devices, which is in the same order of magnitude (10^{-1}) as mobilities reported with solution-processable FETs[80,81,82].

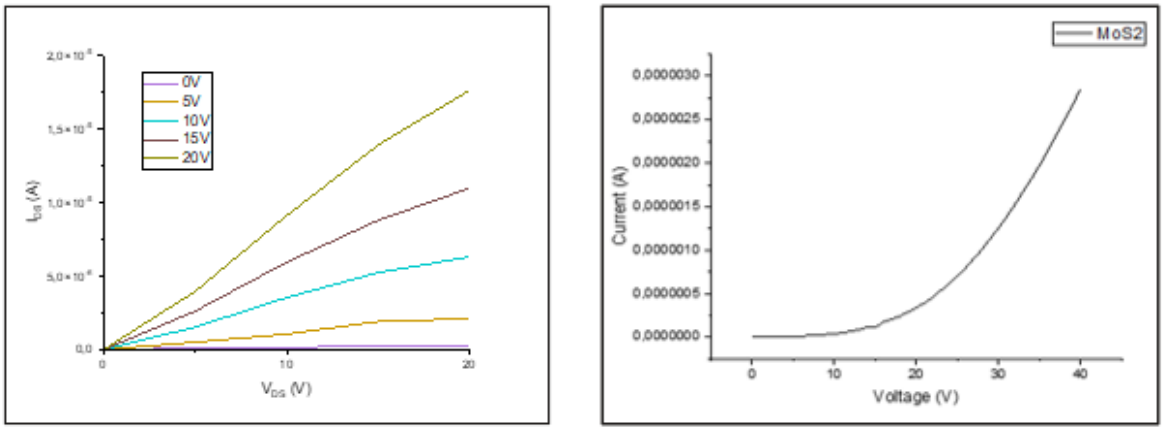

Figure 26. Output and transfer curves of a MoS_2 based n-type FET

Then, to see the effect of the dopant agent in this devices, Nb-doped MoS_2-based FETs have been tested as n-type and p-type devices. First, output curves of n-type FETs at different Nb concentrations (Figure 27) show that n-type FET behavior is maintained at 0.25% and 0.5% Nb atomic concentration but the electron mobility decreases compared to undoped MoS_2 (Figure 28). However, from 0.75% Nb onwards the n-type FET behavior of MoS_2 is lost probably due to the progressive conversion to a p-type material, consistent with PEC results. Therefore, electron mobility of these samples could not be reliably obtained.

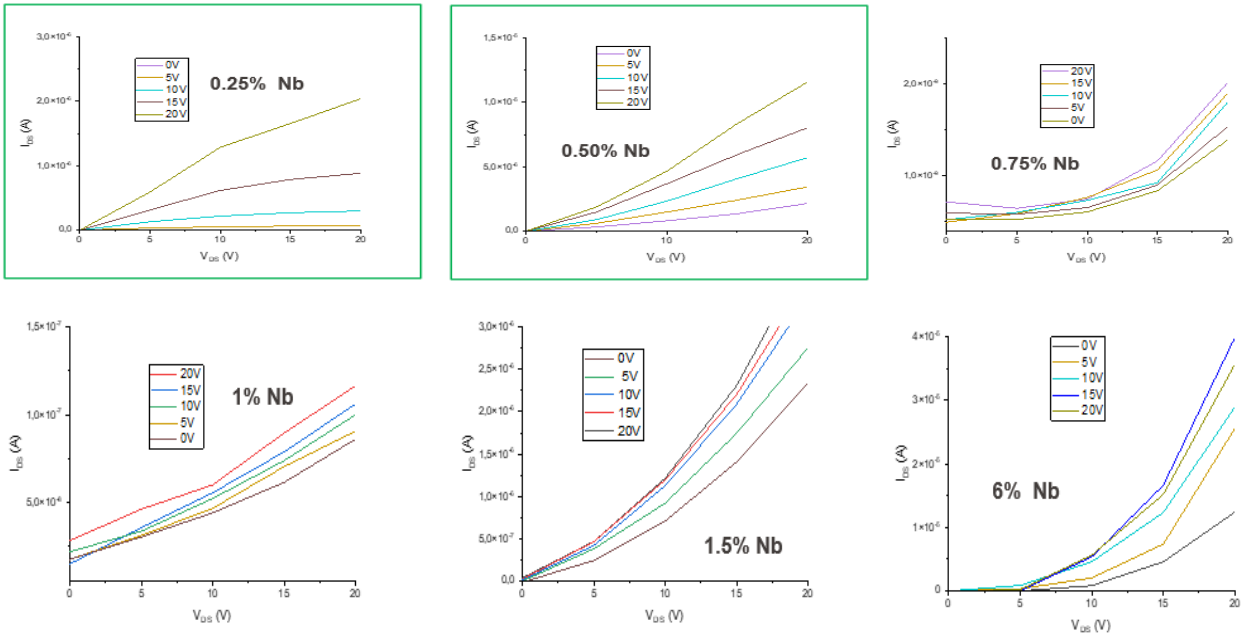

Figure 27. Output curves of Nb-doped MoS_2 based FETs

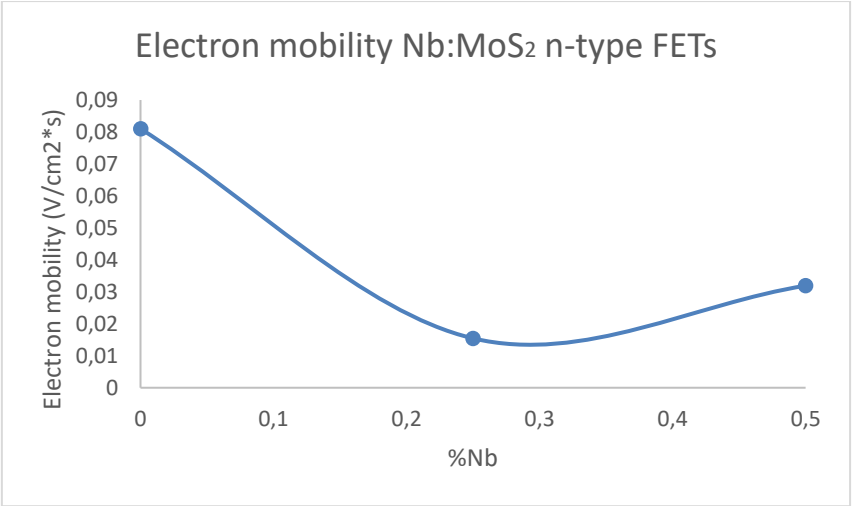

Figure 28. Electron mobility of undoped and Nb-doped MoS_2 based n-type FETs

Then, p-type FETs output curves were obtained by testing the same devices at negative voltages (Figure 29). Here, un-doped MoS_2 is able to conduct current at p-type conditions but it does not show a perfect field effect and the same occurs for 0.25% Nb sample. Interestingly, 0.5% Nb-doped MoS_2 output curve improves and shows a behavior close to a p-type FET. However, from 0.75% Nb onwards the possible p-type FET behavior of MoS_2 is lost, which may suggest that flake thickness of these samples is too high for this application or the negative effect of degenerated p-type doping. The hole mobilities of undoped, 0.25% and 0.5% Nb doped MoS_2 FETs have been calculated (Figure 30) but they may not be considered completely reliables due to the shape of the output curves.

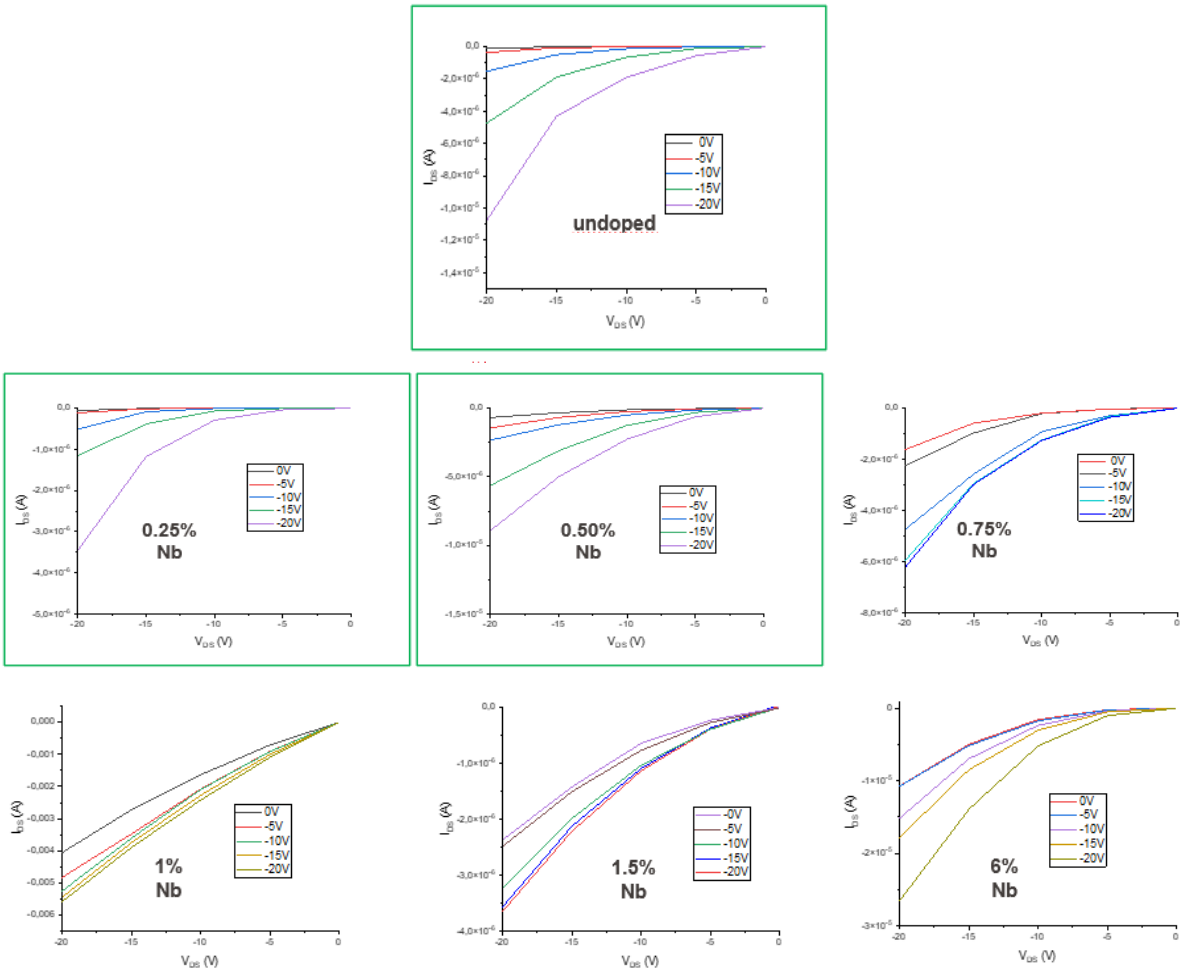

Figure 29. Output curves of Nb-doped MoS_2 based p-type FETs.

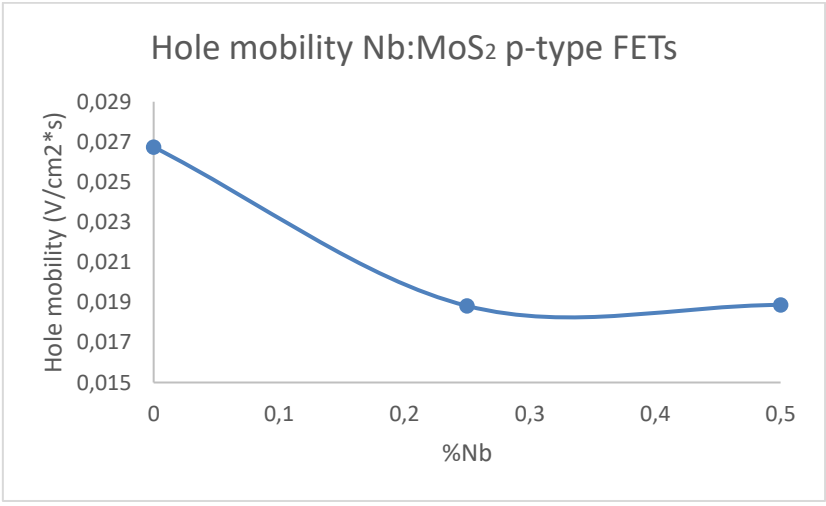

Figure 30. Electron mobility of undoped and Nb-doped MoS_2 based p-type FETs

In summary, notable changes in MoS_2 optoelectronic properties are experienced with Nb doping. Red shiftings of doped samples in PL spectra suggest a reduction of MoS_2's bandgap, aligned with UV-Vis spectroscopy results. Then, from 0.75% Nb onwards MoS_2 is given an ambipolar behavior so that the doped material becomes promising as a photoelectrode for water splitting in a PEC cell. Here, the highest photoactivity is reached at 1% Nb. Finally, 0.5% Nb doped MoS_2 could be promising for ambipolar FETs, as it maintains the field effect of MoS_2 at n-type conditions and shows and seems to show this field effect also at p-type conditions.

Chapter 4 Nb-doping in other TMDs (WSe_2, WS_2)

Once it has been proven that Nb addition to MoS_2 modifies its structural and optoelectronic properties, an initial overview about Nb effects to other highlighted TMDs (WSe_2 and WS_2) was demonstrated. Same as with MoS_2, Nb-doped WSe_2 and WS_2 pellets and thin films have been characterized and their optoelectronic properties tested.

Regarding dopant agent atomic concentrations, for WSe_2 Nb-doping at 0.2% and 0.5% atomic has been demonstrated to enhance its optoelectronic properties such as photoresponsivity[53,54]. For WS_2, low Nb concentrations around 0.5% have been reported to be sufficient to see changes in the material's bandgap and therefore in photoluminescence[83,84].

Considering these references and the promising results seen in MoS_2 around 1% Nb doping, Nb atomic concentrations of 1% and 6% (to see the effect at higher dopant agent concentrations) were tested in WSe_2 and WS_2.

4.1 Nb-doped WSe_2 and WS_2 pellets and thin films characterization

The described scalable methods used to obtain undoped and Nb-doped MoS_2 can also be applied to WSe_2 and WS_2 as they also possess a layered structure. However, for WSe_2 the pellet's annealing process should be performed with Se powder inside the tubes instead of S powder as in MoS_2 or WS_2.

First of all, the crystal structure of the WSe_2 and WS_2 pellets before and after Nb-doping was analyzed by XRD. Figure 31a shows a decrease in intensity between WSe_2 undoped and Nb doped samples due to Nb effects in crystallinity and a new emergent phase in WSe_2 crystal structure when it is doped with 6% Nb as the new peak at 40θ indicates.

On the other hand, XRD spectra of undoped and Nb-doped WS_2 powders in Figure 31b also show an intensity decrease between undoped and doped samples due to crystallinity loss but no new crystal phases are found in Nb-doped WS_2.

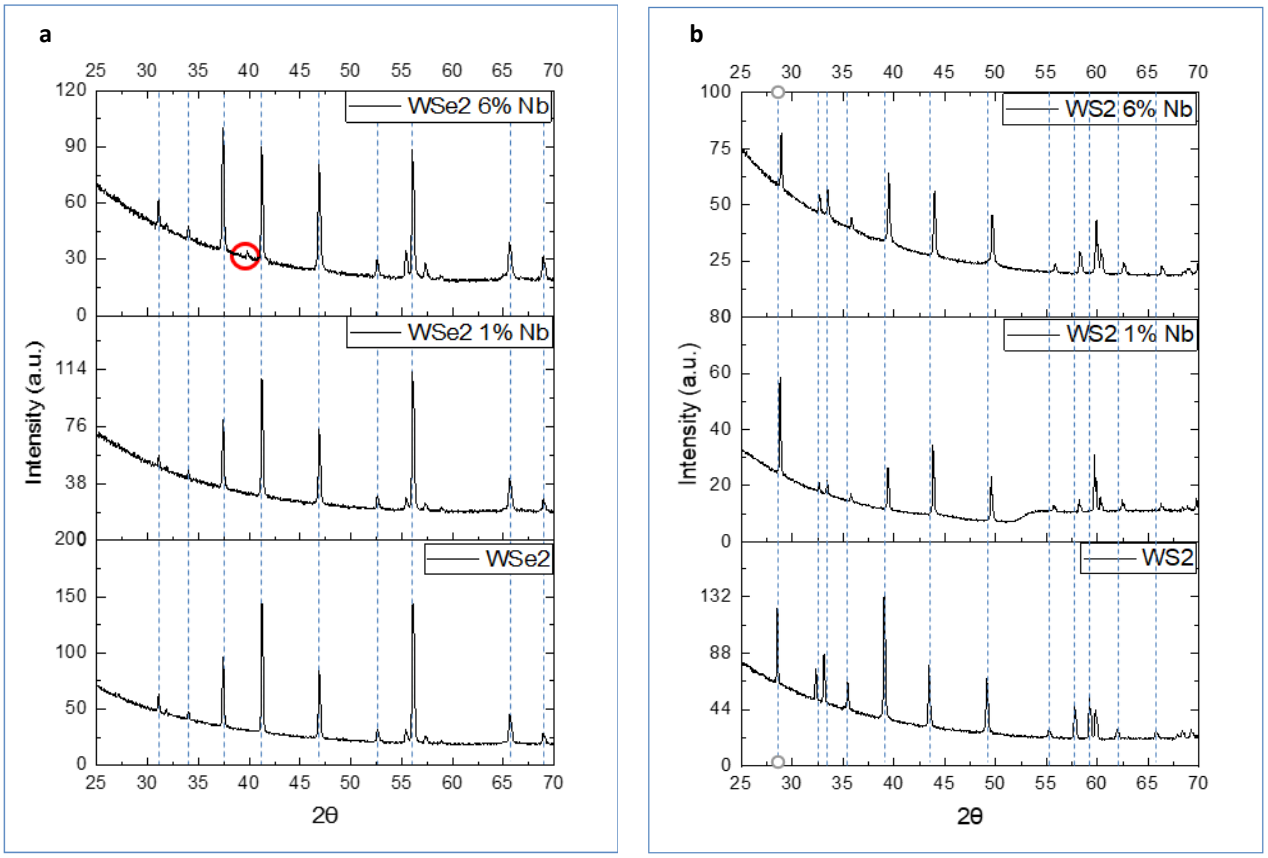

Figure 31. (a) XRD spectra of undoped and Nb-doped WSe_2 powders. (b) XRD spectra of undoped and Nb-doped WS_2 powders.

Furthermore, the lattice parameters of undoped and Nb-doped WSe_2 and WSe_2 (a, c) have been calculated from XRD analysis (Figure 32). For WSe_2 there seems to exist a clear trend between the expansion of lattice constants of WSe_2 and Nb atomic concentration (but more intermediate concentrations should be analysed) while for WS_2 an expansion of lattice parameters occurs at 1% Nb but then it goes down at 6% Nb. Same to MoS_2, these changes could be attributed to the incorporation of Nb atoms to the lattice which lead to new structures such as NbS_2 or other stacking configurations.

We note that, lattice constants of undoped WS_2 were extracted from literature as the measurement was inconclusive.

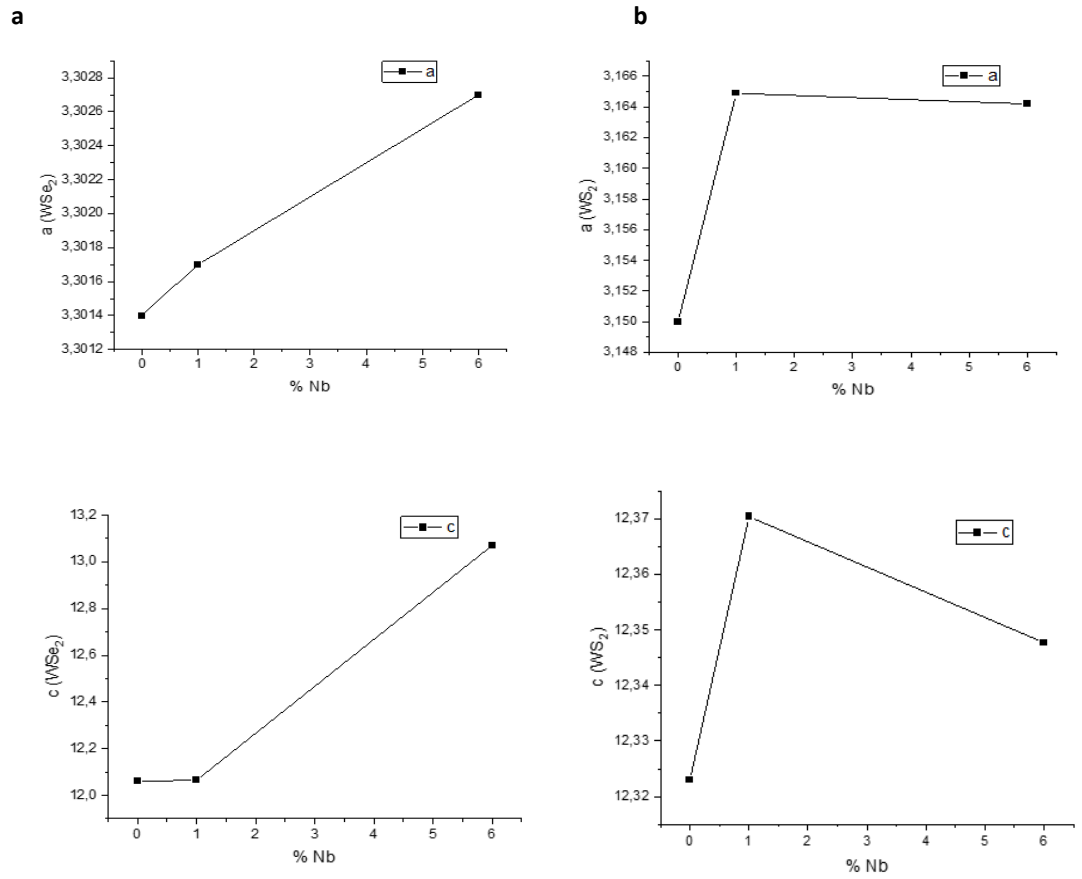

Figure 32. (a) Evolution of WSe_2 lattice parameters at different Nb doping concentrations. (b) Evolution of WS_2 lattice parameters at different Nb doping concentrations[1]

Then, as Nb incorporation also affects the WSe_2 and WS_2 crystal structures, changes in their conductivity are expected due to impurities and delocalized charges introduced. Similar to MoS_2, a decrease in this parameter is expected due to the addition of delocalized charges in WSe_2 structure due to Nb addition.

Resistivity and sheet resistance of WSe_2 and WS_2 undoped and doped pellets were measured (WS_2 6% Nb pellet did not resist the annealing process due to its fragility so both pellet and films measurements could not be done) and the obtained results are shown in Figure 33. Here, conductivity of both TMDs strongly increases between undoped and Nb-doped samples. For WSe_2 the behaviour observed in MoS_2 is reproduced as higher Nb concentrations do not enhance drastically pellet's conductivity.

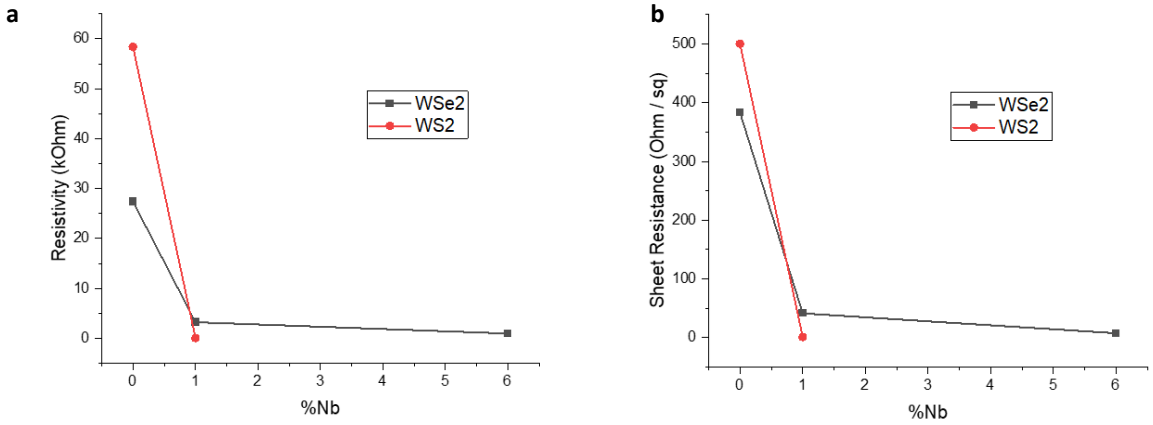

Figure 33. (a) Resistivity of undoped and Nb-doped WSe_2 and WSe_2 pellets. (b) Sheet resistance of undoped and Nb-doped WSe_2 and WSe_2 pellets

After demonstrating the successful incorporation of Nb atoms into the WSe_2 and WS_2 crystal lattices, THA^+ intercalation and exfoliation process was performed. The resulting nanoflake dispersions were then processed into thin films using LLISA deposition as previously described.

First, Raman spectra of undoped WSe_2 films (Figure 34a) display a sharp peak at 254 cm^{-1}, while Nb-doped samples peaks seem to be slightly right-shifted even though it cannot be clearly confirmed because of peak broadening. Indeed, these peaks broadening is caused by an increase in the distribution of photon energy states due to a disruption of WSe_2 crystal lattice[85] as a result of Nb-doping, confirmed by XRD analysis. On the other hand, for WS_2, the main change between undoped and Nb-doped samples (Figure 34b) is the increase in the intensity ratio of the A'_{1g} vibrational mode (422 cm^{-1}) with respect to the E_{2g}. becomes more intense. According to a study by Priyanshu R. et al.[86] this could be attributed to the reduction of sulfur vacancies thanks to the Nb-S binding or to the increased thickness of the doped WS_2 nanoflakes[87].

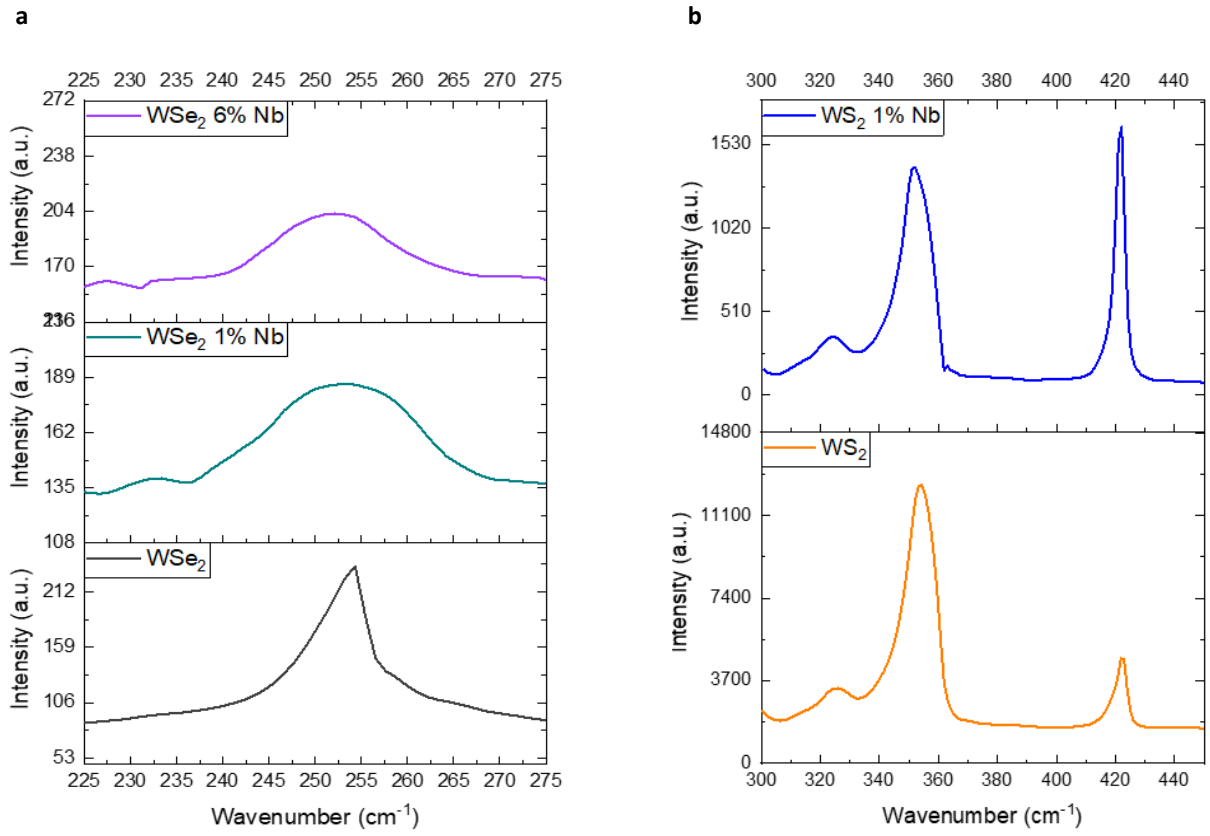

Figure 34. (a) RAMAN spectra of undoped and Nb-doped WSe_2 films. (b) RAMAN spectra of undoped and Nb-doped WS_2 films

Additionally, UV-Vis spectra show the main absorption peak of undoped WSe_2 at 762 nm (Figure 35a). Then, a progressive blue shifting is observed for 1% Nb-doped WSe_2 (759nm) and for 6% Nb-doped WSe_2 (752nm) which gives a sign that WSe_2 bandgap is getting bigger due to the addition of Nb. Furthermore, undoped WSe_2 peak looks sharper than doped samples ones (specially at 6% Nb) so it could be a sign that doped flakes are thicker.

Regarding WS_2, 1% Nb doped spectrum (Figure 35b) shows a clear red-shifting of both absorption peaks, suggesting that the flakes may have larger lateral dimensions (according to the red shifting at 400 nm) and they are thicker (according to the red shifting at 700 nm).

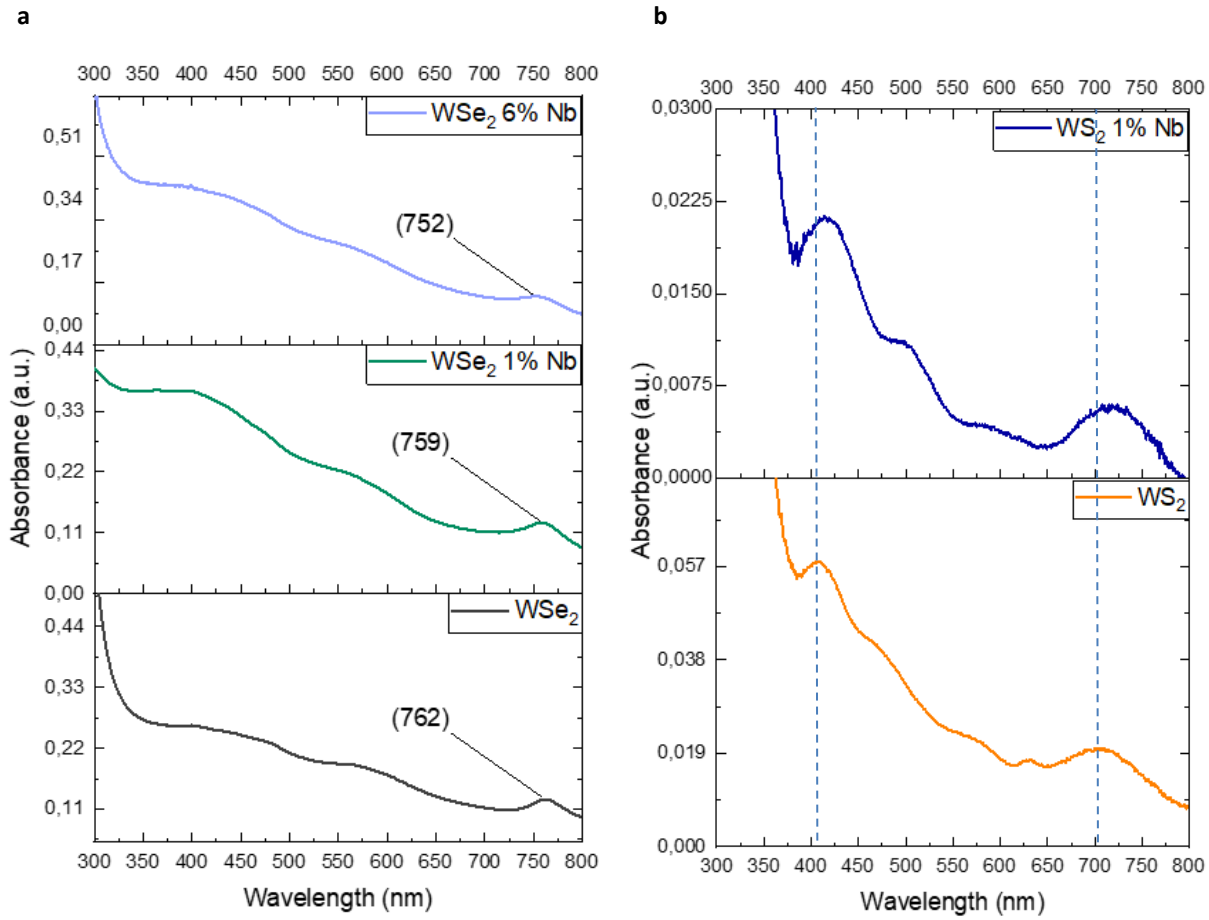

Figure 35. (a) UV-VIS spectrums of undoped and Nb-doped WSe_2 films. (b) UV-VIS spectrums of undoped and Nb-doped WS_2 films

4.2 Nb-doped Wse_2 and WS_2 films optoelectronic properties

Considering the existing differences between undoped and Nb-doped WSe_2 and WS_2, changes in other optoelectronic properties are expected. Therefore, PL spectroscopy and PEC tests have been applied in order to verify changing behavior in TMDs photoactivity and charge separation.

First, undoped and Nb-doped WSe_2 PL spectra (Figure 36a) demonstrate strong photoluminescence in all samples. Here, the main difference between undoped and doped samples is an increase in PL intensity in 6% Nb doped WSe_2, which could be attributed to the existence of more recombination centers created by the defects formed by doping. On the other hand, undoped WS_2 exhibits a sharp PL peak at around 625nm (Figure 36b) while 1% Nb-doped sample PL peak is broadened with respect to the undoped sample's peak, suggesting weaker PL.

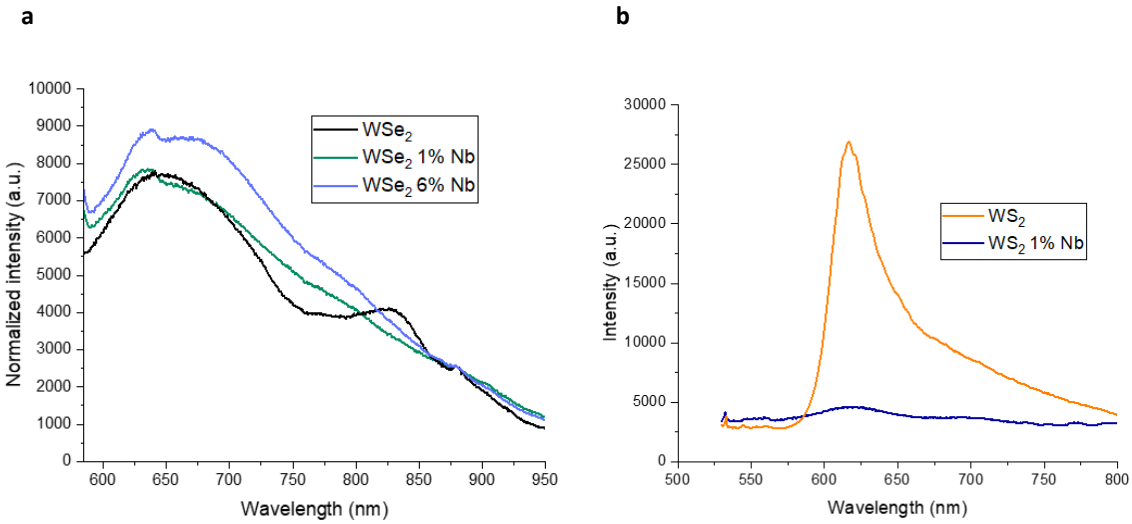

Figure 36. (a) PL spectroscopy of undoped and Nb-doped WSe_2 films. (b) PL spectroscopy of undoped and Nb-doped WS_2 films

Finally, undoped and Nb-doped WSe_2 and WS_2 films were also tested as photoelectrodes inside PEC cells. As Wse_2 has a strong intrinsic p-type behavior and Nb is also a p-type dopant, these TMD based films have only been tested at aqueous conditions. By contrast, WS_2 has intrinsic a n-type behavior but the addition of a p-type dopant as Nb could turn its behavior to p-type taking as a reference the results obtained with MoS_2 in Chapter 3. Therefore, undoped and Nb-doped WS_2 films have been tested in both non-aqueous and aqueous electrolytes to test the n-type and p-type behavior, respectively.

In aqueous conditions, undoped WS_2 is able to carry perform HER under illumination, as a current change and photoactivity are seen at negative voltages (Figure 37a). However, the addition of 1% Nb and specially 6% Nb causes a decay in photoactivity, which could be because of the rise of defect sites after Nb incorporation. Moreover, neither undoped nor Nb-doped WS_2 samples display photoactivity (Figure 37b).

However, LSV applied at non-aqueous conditions to undoped and Nb-doped WS_2 films (Figure 38) confirms the natural n-type behaviour of undoped WS_2 as it shows photoactivity at positive voltages. However, Nb-doping is not beneficial for WS_2 performance in non-aqueous conditions as the sample shows reduced photoactivity.

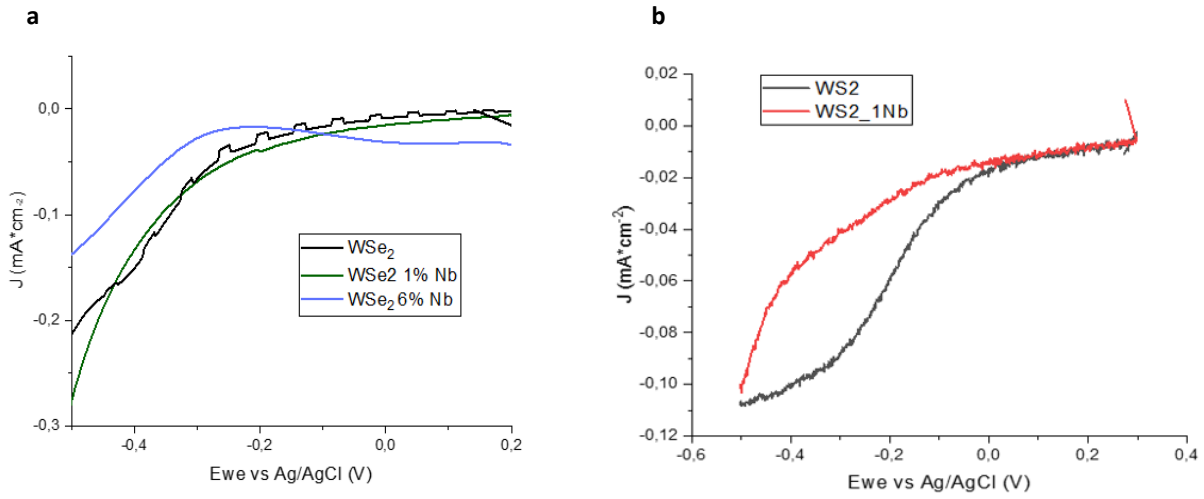

Figure 37. (a) LSV results in aqueous conditions with undoped and Nb-doped WSe_2 films. (b) LSV results in aqueous conditions with undoped and Nb-doped WS_2 films

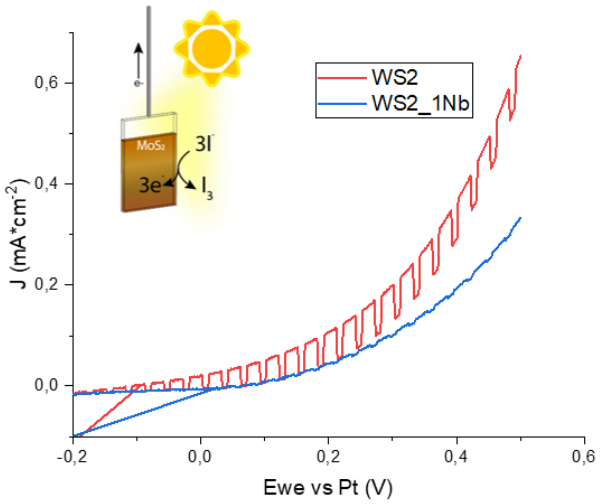

Figure 38. LSV in non-aqueous conditions of undoped and Nb-doped WS_2 films

In summary, Nb-doping in WSe_2 and WS_2 has been confirmed in pellets (according to distortions on the TMDs' crystal structures) and thin films (according to shiftings in Raman and UV-Vis spectroscopies). Additionally, the electronic bandgap of these TMDs is tuned, getting bigger for WSe_2 and smaller for WS_2 according to red-shiftings in UV-Vis and PL spectroscopies. Consequently, the optoelectronic properties of WSe_2 and WS_2 are modified, obtaining enhanced photoluminescence intensity for $Nb_{0.06}WSe_2$. However, as it stands no improvements have been found in PEC performance of these TMDs after Nb-doping. Finally, THA^+ intercalation method is demonstrated to be suitable for undoped and Nb-doped WSe_2 and WS_2 exfoliation.

Chapter 5 Rhenium (Re) doping in MoS_2: An initial study.

In Chapter 3 it was demonstrated that the addition of a p-type dopant Nb to MoS_2 crystal lattice gives an additional p-type behaviour to the TMD. Furthermore, the addition of a n-type dopant to MoS_2 could enhance the n-type behaviour of the TMD and potentially improve its photoelectrochemical performance in non-aqueous conditions.

Among the transition metals which act as n-type dopants, Rhenium (Re) has been suggested theoretically[58] to be the most suitable for MoS_2 as the activation energy needed is the lowest with this dopant agent.

Then, Re-doped MoS_2 pellets and films have been synthetized using the same methods as with Nb-doped MoS_2. Taking as a reference the study reported by Yuanyuan Li et al.[61], where 0.6% Re doping was enough to modulate optoelectronic properties of MoS_2, samples with 0.5%, 1% and 5% Re:Mo atomic content were tested.

An initial study regarding characterization and optoelectronic properties testing of these samples is shown in the following sections.

5.1 Characterization of Re-doped pellets and films

First of all, resistivity of all Re-doped pellets was tested as an indirect way of seeing the initial effects of Re on the MoS_2 crystal structure. As expected, there is a drastic increase in conductivity from undoped MoS_2 to Re-doped MoS_2 pellets even at low dopant agent percentages. Besides, conductivity keeps increasing as long as higher Re concentrations are added to the TMD crystal structure (Figure 39). In contrast, more conductive pellets are obtained with Nb doping at the same theoretical concentrations. This could be expected because Nb's electrical conductivity (6.7×10^6 S/m) is greater than Re's conductivity (5.6×10^6 S/m), both values at 293K.

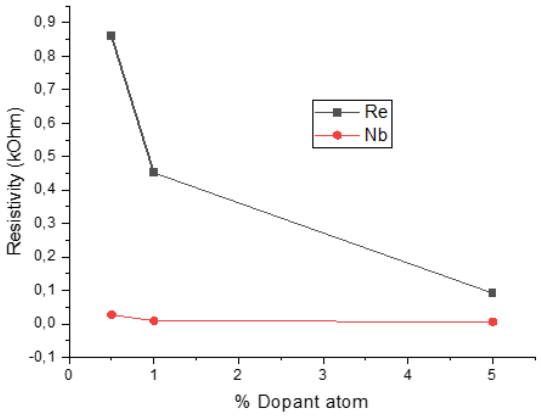

Figure 39. Resistivity of MoS_2 pellets doped with Nb or Re

Due to increased pellet fragility with the addition of Re, only 0.5% and 1% Re-doped samples were able to resist THA^+ intercalation while the 5% Re-doped MoS_2 pellet quickly dissolved.

Moving on to thin film characterization, Raman spectra of undoped and Re-doped MoS_2 are shown in Figure 40. As expected from literature[88], Re-doped samples display red-shifted peaks compared to undoped samples and this shifting seems to increase at higher dopant agent concentrations due to more distortion in MoS_2 crystal structure.

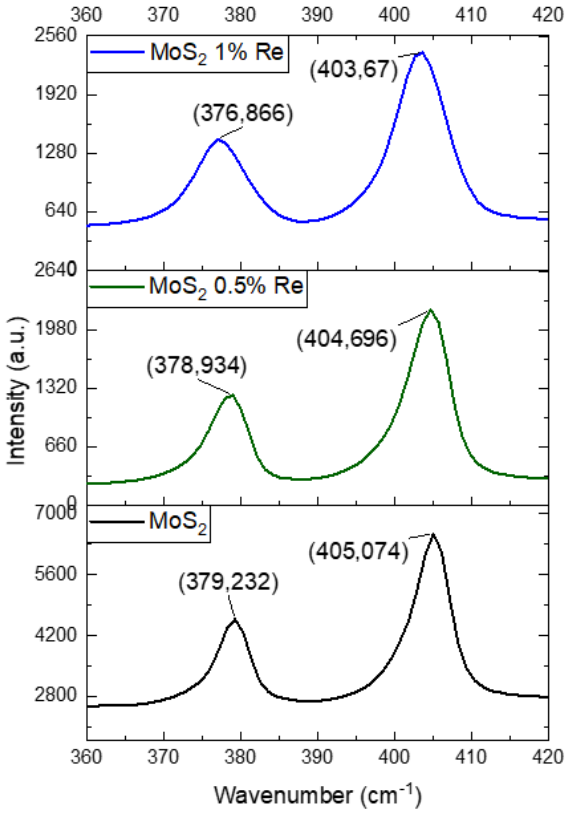

Figure 40. RAMAN spectrums Re-doped MoS_2 films

UV-Vis spectra show red-shifted excitonic A and B peaks for 0.5% Re-doped MoS_2 (Figure 41) compared to undoped MoS_2, suggesting a larger bandgap for the doped samples. However, excitonic peaks C and D at low wavelengths are blue-shifted compared to the undoped sample, suggesting smaller lateral sizes. As seen in Chapter 2, MoS_2 also experiences similar changes when it is doped with Nb. Furthermore, the intensity of the excitonic peaks at high wavelengths decreases when Re concentration increases. Possibly this is due to a phase change of MoS_2 from semiconducting 2H to semi-metallic 1T caused by electron injection into MoS_2 crystal lattice by Re atoms. This phase transition was reported by Guoping Gao et al.[89] after an electrochemical electron injection into MoS_2 and also occurs during Li^+ electrochemical intercalation[46]. However, this statement should be confirmed by XRD analysis.

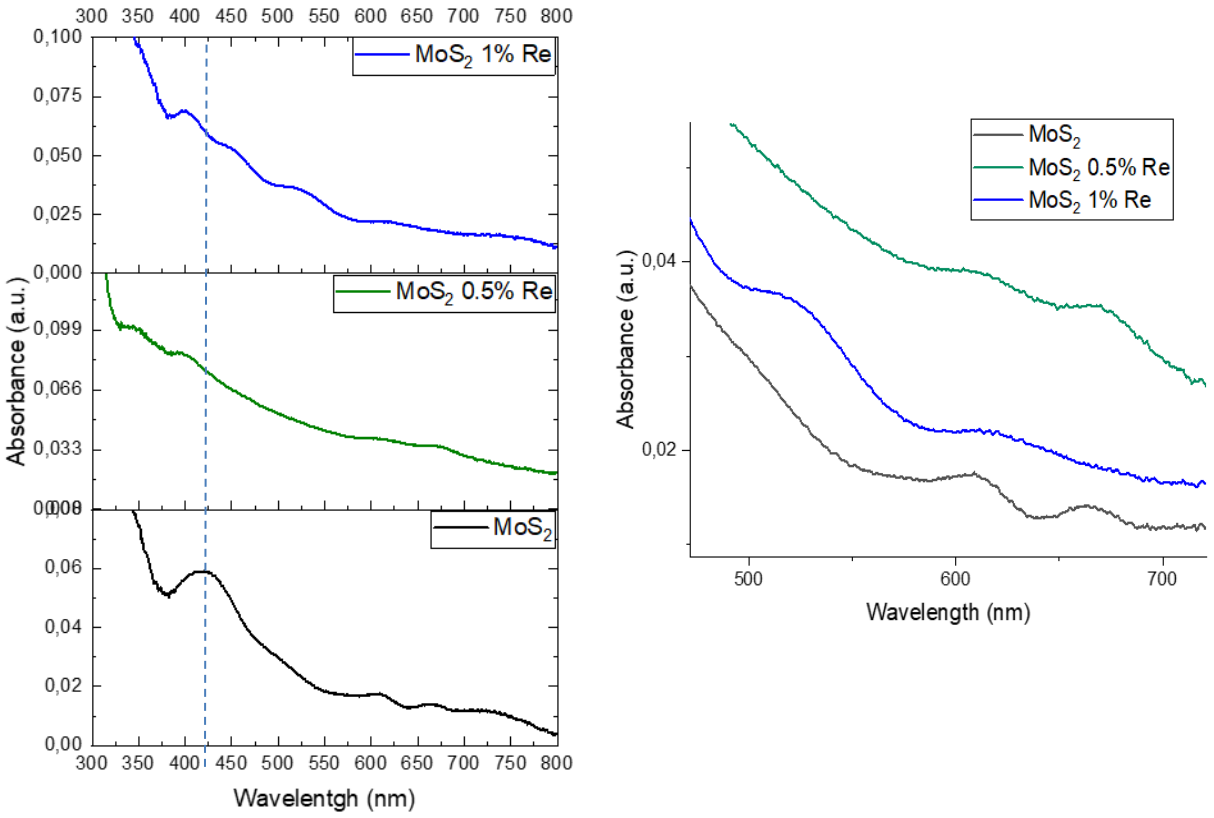

Figure 41. UV-Vis spectra of undoped and Re-doped MoS_2

Shifting between undoped and Re-doped MoS_2 thin films were observed in both Raman and UV-VIS spectra, suggesting successful incorporation of the Re atom into the MoS_2 crystal lattice. As such, additional differences in optoelectronic properties can also be expected. Therefore, photoluminescence and photoelectrochemical performance in non-aqueous conditions were tested.

Looking at Figure 42, the 0.5% Re-doped MoS_2 spectrum shows a similarly intense photoluminescence as undoped MoS_2 and a main PL peak (713 nm) red-shifted compared to undoped one (668 nm). Furthermore, the 0.5% Re-doped sample shows an additional PL peak at around 625 nm corresponding to the B exciton, suggesting thicker nanoflakes[91], together with the peak shifting implies a widening of the bandgap. Moreover, 1% Re-doped MoS_2 shows two PL peaks but they

are broadened and their intensity decreased compared to 0.5% Re-doped and undoped MoS_2 films, probably because of too quick charge recombination.

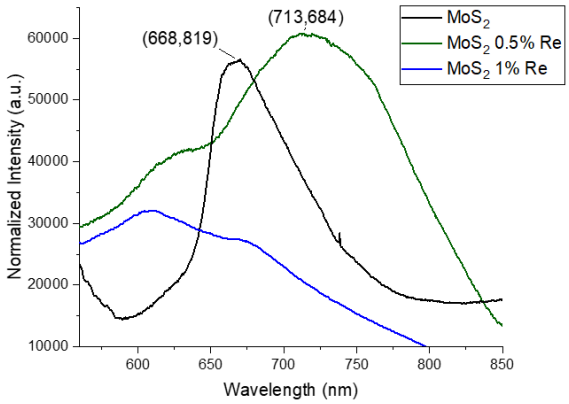

Figure 42. PL spectra of undoped and Re-doped MoS_2

Finally, Re-doped films were tested as photoelectrodes in a PEC cell at non-aqueous conditions to examine their n-type behaviour, as described in Chapter 3. Figure 43 shows the results of LSV and OCV applied to all samples, where n-type doping of MoS_2 does not enhance undoped sample PEC performance in non-aqueous conditions as photoactivity is clearly reduced.

Moreover, OCP tests confirm that Re-doped samples perform the oxidation reaction under illumination, however the photo potential is hindered compared to undoped MoS_2, probably because of the previously mentioned phase transition to semi-metallic 1T.

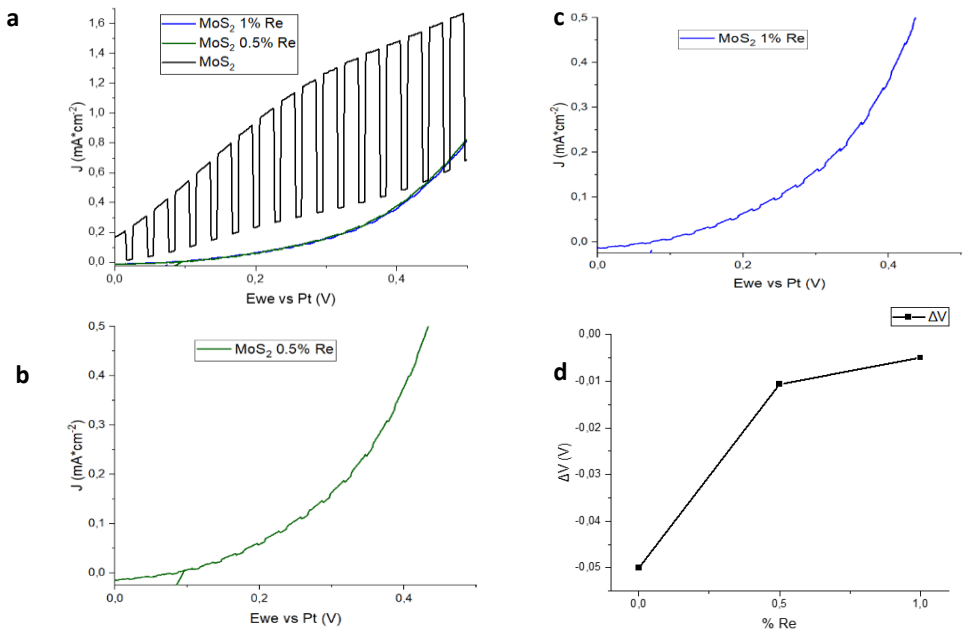

Figure 43. (a) LSV in non-aqueous of undoped and Re-doped MoS_2. films. (b) Zoom of LSV results of 0.5% Re doped MoS_2 film. (c) Zoom of LSV results of 1% Re doped MoS_2 film. (d) Potential change evolution during OCV along %Re

In summary, Re-doped MoS_2 pellets are more conductive than undoped MoS_2 suggesting that Re is present in MoS_2 structure. Furthermore, shifting in Raman and UV-VIS spectroscopy of Re-doped MoS_2 thin films suggest the presence of Re atoms in the TMD. This statement is supported by the modification of the MoS_2 bandgap, which gets smaller according to a red-shifting in the PL peak compared to undoped MoS_2. Therefore, MoS_2's optoelectronic properties are modified due to Re-doping but not enhanced for PEC applications.

Chapter 6 Conclusions and future work

6.1 Conclusions

In conclusion we demonstrate a unique and scalable, solution processable approach for producing doped 2D TMDs.

We show that his approach is applicable for a range of TMDs including MoS_2, WSe_2 or WS_2. Furthermore, this approach can be used to introduce different dopant atoms depending on the desired properties. Finally, we presented detailed characterization of the materials, showing the evolution of optoelectronic properties as a function of dopant atom concentration.

6.1.1 Nb doping of MoS_2

The study of Nb-doped MoS_2 pellets confirms Nb incorporation to MoS_2 structure thanks to ICP-MS and XRD analysis. Indeed, Nb doping makes MoS_2 more conductive, less crystalline and modifies its lattice parameters. Furthermore, a new crystal phase is detected at 6% Nb atomic concentration.

Nb presence in MoS_2 thin films is confirmed by Raman and UV-Vis spectroscopy, where clear trends between peak shifting and dopant atom concentration are observed. Consequently, the optoelectronic properties of MoS_2 are modified by Nb incorporation. Red shiftings in PL spectra from 0.25% Nb to 0.75% Nb and red-shiftings in UV-VIS spectroscopy peaks of all Nb-doped samples suggest that the bandgap of MoS_2 is decreased with increasing amounts of Nb.

Regarding PEC performance in non-aqueous conditions, Nb doping is not beneficial for MoS_2 as it reduces the material's photoresponsivity at these conditions by diminishing its intrinsic n-type behavior. By contrast, Nb doping from 0.75% onwards enables MoS_2 to perform in acid conditions by giving p-type behavior to the material, becoming ambipolar depending on the conditions. The highest photoactivities in acid conditions are found with 1% and 1.5% Nb doping.

Finally, ultra-thin MoS_2 based n-type field effect transistors by solution processable methods were successfully obtained with an electron mobility of 0.08102 $cm^2/V{\cdot}s$.
At n-type conditions, Nb doping at 0.25% and 0.5% Nb maintain the behavior of the undoped device but decreases the electron mobility due to increased p-type behavior. Indeed, doping at 0.75% Nb onwards affects negatively to the n-type FET behavior of MoS_2. Interestingly, 0.5% Nb doping seems to enable MoS_2 to perform as a p-type FET, so that this doping percentage becomes promising to reach ambipolar (n-type and p-type) FETs. Finally, 0.75% and higher Nb percentages affect negatively to p-type FET behavior of MoS_2 due to the negative effects of degenerative doping and flake thickness.

6.1.2 Nb-doping of WSe_2 and WS_2

The XRD analysis of Nb-doped WSe_2 pellets reveals Nb incorporation into the TMD crystal lattice, which expands its lattice parameters and also enhances its conductivity. Regarding Nb-doped thin WSe_2 films, shiftings in Raman and UV-Vis peaks confirm the presence of the dopant agent in the nanoflakes.

Furthermore, Nb doping of WSe_2 did not appear to have detrimental effects on the PL response. Regarding bandgap tuning, UV-Vis spectroscopy shows a blue shifting of the excitonic peak which suggests an increase of the bandgap of WSe_2. Finally, WSe_2 PEC performance in acid conditions is not improved after Nb addition as there is a decrease in photoactivity.

Regarding Nb doping in WS_2, the dopant agent can be detected in the TMD crystal structure via XRD, showing modifications in lattice parameters. Increased conductivity is also noted. Nb-doped (1%) WS_2 thin films also show shiftings in Raman and UV-VIS spectroscopy peaks compared to undoped WS_2. Red shifting of the main excitonic peaks peak suggests a bandgap shrinking as a result of doping WS_2 with Nb. Finally, Nb doping does not improve n-type PEC properties of WS_2, nor did it give sufficient p-type behavior to perform the HER reaction in acidic conditions. We note that only one Nb atomic percentage could be tested and that additional tuning could allow for similar behavior observed when doping MoS_2.

6.1.3 Re-doping of MoS_2

The initial study about n-type doping with Re to MoS_2 gives evidence that the dopant agent is incorporated to the TMD. First, analysis of the pellet resistivity shows enhanced conductivity in doped samples. Then, Re is also detected in doped MoS_2 films as a left shifting in Raman spectroscopy and a red shifting in UV-Vis spectroscopy is seen in doped samples. Besides, red-shifting of 0.5% Re-doped MoS_2 PL peak together with the UV-Vis shifthing suggests a shrinking of the MoS_2 bandgap, similar to behavior observed with Nb doping. Additionally, the intensity of excitonic peaks decreases with increased Re concentrations. This may suggest the disappearance of the semiconducting 2H behavior and the emergence of the semi-metallic 1T phase. Finally, Re-doping in MoS_2 at 0.5% and 1% atomic does not improve performance in PEC cells at non-aqueous conditions. This would agree with the previous statement that Re may be injecting electrons thus inducing a phase change in the MoS_2 crystal structure.

6.2 Future work

This thesis has provided an intensive study about Nb doping in MoS_2 and how different dopant concentrations affect this TMD's structure and properties. However, this study could be further improved with an accurate and direct analysis about the evolution of MoS_2 bandgap along different dopant concentrations, as this is a key property for optoelectronic applications. Tools such as XPS and UPS would be invaluable. We note that initial experiments were conducted but required intensive analysis which were not able to be completed within the time frame of this thesis. Future work will complete these analyses.

Additionally, now that it has been demonstrated that Nb-doped MoS_2 ambipolar ultra-thin FETs by solution processable methods can be achieved it will be interesting to work on enhancing its mobility. For example, adding a protective layer of SiO_2 or PMMA could help to increase electron and hole mobility according to what is reported in literature. Indeed, enhancing hole mobility would make way for ultra-thin MoS_2 to be incorporated into ultra-thin, flexible devices in new ways. One example of this is a hole transport layer in the perovskite solar cell[92].

Regarding WSe_2 and WS_2, the initial approach made could be continued by testing new Nb atomic percentages according to the behavior seen previously, giving a thorough review about how the dopant agent concentration affects these TMDs properties. Also, the initial study of Re doping in MoS_2 could be extended to these materials, particularly for testing in high-mobility field effect transistors due to their high conductivity. This could provide a broader range of ambipolar materials.

Furthermore, this project gives more evidence of the suitability of THA^+ intercalation and exfoliation method to reduce TMDs number of layers. From this point, a study about the influence of several parameters such as intercalation time or voltage applied in the morphology or properties of the obtained films will be necessary to better understand the process and therefore adapt it to a broader range of layered materials.

7. SUPPLMENTARY INFORMATION

7.1. METHODS

ELECTROCHEMICAL INTERCALATION WITH THA^+ AND EXFOLIATION

The TMD pellet and a graphite electrode, which work as a cathode and as an anode respectively, are submerged in an electrolyte solution (40mL ACN + 200mg THAB). Then, voltage (10V) is applied and the intercalation of THA^+ occurs at the TMD electrode while an oxidation reaction (Br^- to Br_2) is produced at the graphite electrode, as each atom of THA^+ intercalated requires one electron from the external circuit to balance the charge (Equation 1).

$$MoS_2 + xTHA^+ \rightarrow (THA^+)xMoS_2{}^{x-}$$

$$xBr_2 + \rightarrow \left(\frac{x}{2}\right) Br_2 + xe^-$$

Equation 1. Intercalation and oxidation reactions

These reactions are confirmed by the yellow color that the solution around the graphite electrode acquires and also by the progressive expansion of the pellet to finally reach a fluffy shape when intercalation process comes to an end (normally in 24-48h). Then, the exfoliated pellet is gathered and dissolved in 10mL of NMP to be bath-sonicated at low power for minimum 30 minutes, until the solution looks exfoliated. Afterwards, a centrifugation at 120 rcf for 30 minutes is applied to make precipitate the remaining bulk material and impurities, keeping the supernatant which contains the TMD nanoflakes distribution.

LIQUID-LIQUID INTERFACIAL SOLVENT ASSISTED FILM DEPOSITION

In this film deposition method, the TMD nanoflakes solution is dispersed into the liquid junction layer between two solvents that have to be immiscible between them and with the TMD solution, need to have different densities and a low boiling point.

First, the substrates are put in a vacuum filter and the two layers of solvents (e.g. water and hexane) are put upon them. Then, the nanoflakes solution is carefully injected between the two layers until a uniform film is formed. After the injection, the upper layer is vacuumed and afterwards the lower layer too, allowing the nanoflakes to lay down and stick uniformly upon the FTO substrates avoiding aggregation.

7.2. TECHNIQUES

SHEET RESISTANCE AND RESISTIVITY MEASUREMENTS

Pellet's edge-to-edge resistivity was measured with a multimeter in resistance mode. Sheet resistance was measured by the four probes method, where 2 probes measure a DC current applied through the sample while the 2 others measure the voltage drop. Then, sheet resistance is calculated by the formula $Rs = \frac{\pi}{\ln(2)} \cdot \frac{\Delta V}{I}$

RAMAN AND PHOTOLUMINESCENCE SPECTROSCOPIES

Raman and photoluminescence spectroscopies were developed on a LabRAM HR Raman spectrometer (HORIBA) at 532nm excitation wavelength.

UV-VIS

UV-VIS spectroscopy was carried out by a UV-VIS-NIR UV-3600 (Shimadzu) spectrophotometer.

SEM

SEM images were acquired using a Zeiss Merlin microscope

ICP-MS

ICP-MS analysis was carried out with Agilent Technologies LC Infinity II ICP-MS Triple Quad 8900

XRD ANALYSIS

Dried powders of the samples were examined using a Bruker D8 Discover diffractometer from 0-75° 2θ.

ZETA POTENTIAL ANALYSIS

Zeta potential measurements were carried out by a nanoparticle tracking analysis instrument (ZetaView).

PHOTOELECTROCHEMICAL MEASUREMENTS

TMD films deposited on FTO substrates were used as photocathodes (working electrode) in the three-electrode PEC measurement. In aqueous electrolyte (1M H_2SO_4) with a Pt counter electrode and a Ag/Ag+ reference electrode and in non-aqueous electrolyte (25mM LiI and 50Mm TBAFP in acetonitrile) with a glassy-carbon counter electrode and a Pt reference electrode. Linear scan voltammetry (LSV) measurements were carried out with a BioLogic SP-50 potentiostat with an electrode active area of 0.25 cm^2, applying voltage with a scan rate of 10 mV s^{-1}. Intermittent illumination simulating sunlight was provided by a filtered 450W Xenon lamp.

FET MEASUREMENTS

Output curves of synthetized FETs were obtained by plotting the drain current as a function of drain voltage for different gate voltages. Transfer curves were obtained by plotting the drain current as a function of gate voltage for different drain voltages.

7.3. SUPPLEMENTARY FIGURES AND TABLES

Table 1. ICP-MS undoped and Nb-doped MoS_2 powder

Sample	Mo (ppm)	Nb (ppm)	% Nb
Undoped Powder	23,6	0,04	0,178
0.25% Nb	28,94	0,06	0,197
0.5% Nb	29,68	0,09	0,296
1% Nb	29,55	0,41	1,391
6% Nb	30,91	1,63	5,284

Table 2. ICP-MS of undoped and Nb-doped MoS_2 flakes

Sample	Mo (ppm)	Nb (ppm)	% Nb
Undoped Flakes	1,04	- (<LOD)	0
0.25% Nb (F)	1,75	- (<LOD)	0
0.5% Nb (F)	1,39	0,01	0,391
1% Nb (F)	9,65	0,11	1,127
6% Nb (F)	9,96	0,76	7,657

Table 3. Resistivity and sheet resistance values of undoped and Nb-doped MoS_2 pellets

Sample	Sheet resistivity (Ohm/sq)	Resistivity (kOhm)
MoS_2	9319,44	3320
MoS_2 0.25% Nb	1,2984	0,0424
MoS_2 0.5% Nb	1,2282	0,0282
MoS_2 0.75% Nb	0,2276	0,0126
MoS_2 1% Nb	0,2177	0,0096
MoS_2 1.5% Nb	0,2169	0,0080
MoS_2 6% Nb	0,2043	0,00678

Table 4. Zeta potential and particle mobility analysis of undoped and Nb-doped MoS_2 nanoflakes solutions

Sample	ZP (mV)	Mobility (mum/sec/V/cm)
MoS_2	-21,36	-1,62
MoS_2 0.25% Nb	-15,42	-1,18
MoS_2 0.5% Nb	-7,18	-0,55
MoS_2 0.75% Nb	-19,14	-2,70
MoS_2 1% Nb	-35,26	-2,68
MoS_2 1.5% Nb	-35,58	-2,70
MoS_2 6% Nb	-35,94	-2,73

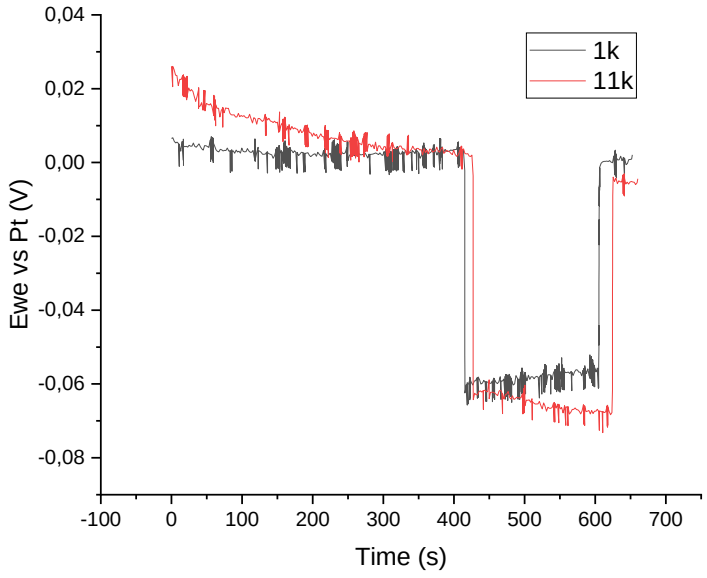

Supplementary Figure 1. OCVs of MoS_2 films from nanoflakes solutions obtained with different centrifugation speed

Table 5. Charge mobilities of undoped and Nb-doped MoS_2 based FETs

Nb content (%)	n-type mobility ($cm^2/V*s$)	p-type mobility ($cm^2/V*s$)
0	0,08102	0,02674
0.25	0,01545	0,01882
0.5	0,03191	0,01887

Table 6. Undoped and Nb-doped WSe_2 resistivity and sheet resistance

Sample	Resistivity (kOhm)	Sheet resistance (Ohm/sq)
WSe_2	27,4	383,18
WSe_2 1% Nb	3,22	41,59
WSe_2 6% Nb	0,96	7,69

Table 7. Resistivity and sheet resistance of undoped and Nb-doped WS_2 pellets

Sample	Resistivity (kOhm)	Sheet resistance (Ohm/sq)
WS_2	58,40	500,20
WS_2 1% Nb	0,0484	1,26

Table 8. MoS_2 Re doped pellets resistivity analysis

Sample	Resistivity (kOhm)
MoS_2	3320
MoS_2 0.5% Re	0,860
MoS_2 1% Re	0,452
MoS_2 5% Re	0,0921

References

1. *Novoselov, K. S. et al.* Electric Field Effect in Atomically Thin Carbon Films. Science 306, 666– 669 (2004).
2. *Miró, P. et al.* An Atlas of Two-Dimensional Materials. Chem. Soc. Rev. 43, 6537– 6554 (2014).
3. *Zhang, Y. et al.* Experimental Observation of the Quantum Hall Effect and Berry's Phase in Graphene. Nature, 438, 201– 204 (2005).
4. *Geim, A. K.; Novoselov, K. S.* The Rise of Graphene. Nat. Mater. 6, 183– 191 (2006).
5. *Liu, G.-B. et al.* Electronic structures and theoretical modelling of two-dimensional group-VIB transition metal dichalcogenides. Chem. Soc. Rev. 44, 2643-2663 (2015).
6. *Kang, K. et al.* High-Mobility Three-Atom-Thick Semiconducting Films with Wafer-Scale Homogeneity. Nature 520, 656– 660 (2015)
7. *Park, Y. et al.* Biotunable nanoplasmonic filter on few-layer MoS2 for rapid and highly sensitive cytokine optoelectronic immunosensing. ACS Nano 11, 5697–5705 (2017).
8. *J. Ping et al.* Recent advances in sensing applications of two-dimensional transition metal dichalcogenide nanosheets and their composites. Adv. Funct. Mater., 27 , 1605817 (2017).
9. *Y. X. Yin et al.* Lithium sulfur batteries: Electrochemistry, materials and prospects Chem., Int. Ed.,52 , 13186 — 13200 (2013).
10. *B. Hinnermann et al*. Biometric Hydrogen Evolution: MoS_2 nanoparticles as catalyst for hydrogen evolution. J. Am. Chem. Soc. 127, 15, 5308–5309 (2005)
11. *Ouyang Y. et al.* Activating inert basal planes of MoS_2 for hydrogen evolution reaction through the formation of different intrinsic defects. Chem Mater 28: 4390– 4396 (2016).
12. *Shu H. et al.* Defect engineering in $MoSe_2$ for the hydrogen evolution reaction: from point defects to edges. ACS Appl Mater Interfaces 9: 42688– 42698 (2017).
13. *J. A. Baglio et al.* Electrochemical characterization of p-type semiconducting tungsten disulfide photocathodes. J. Am. Chem. Soc., 1983, 105 , 2246 —2256
14. *Manzeli, S. et al.* 2D transition metal dichalcogenides. Nat. Rev. Mater. 2, (2017).
15. *Liu, G.-B. et al.* Electronic structures and theoretical modelling of two-dimensional group-VIB transition metal dichalcogenides. Chem. Soc. Rev. 44, 2643–2663 (2015)
16. *Bernardi, M. et al.* Extraordinary sunlight absorption and one nanometer thick photovoltaics using two-dimensional monolayer materials. Nano Lett. 13, 3664–3670 (2013).
17. *May, P. et al.* Reinforcement of metal with liquid-exfoliated inorganic nanoplatelets. Appl. Phys. Lett. 103, 163106 (2013).
18. *Zhao, W. et al.* Evolution of Electronic Structure in Atomically Thin Sheets of WS_2 and WSe_2. ACS Nano 7, 791–797 (2013).
19. *Splendiani, A. et al.* Emerging Photoluminescence in Monolayer MoS_2. Nano Lett. 10, 1271–1275 (2010).

20. *Arora, A. et al.* Excitonic resonances in thin films of WSe_2: from monolayer to bulk material. Nanoscale 7, 10421–10429 (2015).
21. *Mak, K. F., Lee, C., Hone, J., Shan, J. & Heinz, T. F.* Atomically thin MoS_2: a new direct-gap semiconductor. Phys. Rev. Lett. 105, 136805 (2010).
22. *Dolui, K. & Sanvito, S.* Dimensionality-driven phonon softening and incipient charge density wave instability in TiS 2. EPL Europhys. Lett. 115, 47001 (2016).
23. *Lüssem, B. et al.* Doping of organic semiconductors. Phys. Status Solidi A, 210: 9-43 (2013).
24. *Aruchami A.* Photoelectrochemistry and Photovoltaics of Layered Semiconductors (1992)
25. *Lee, C.-H. et al.* Atomically thin p–n junctions with van der Waals heterointerfaces. Nat. Nanotechnol. 9, 676–681 (2014).
26. *Zhang, K. et al.* Correction to Manganese Doping of Monolayer MoS_2: The Substrate Is Critical. Nano Lett. 16, 2125 (2016).
27. *Komsa, H.-P.* Effects of confinement and environment on the electronic structure and exciton binding energy of MoS_2 from first principles. Phys. Rev. B 86, (2012).
28. *Jariwala, D et al.* Van der Waals Materials for AtomicallyThin Photovoltaics: Promise and Outlook. ACS Photonics 4, 2962–2970 (2017).
29. *Liu, G.-B., Xiao, D., Yao, Y., Xu, X. & Yao, W.* Electronic structures and theoretical modelling of two-dimensional group-VIB transition metal dichalcogenides. Chem. Soc. Rev. 44, 2643–2663 (2015).
30. *Gusakova et al.* Electronic Properties of Bulk and Monolayer TMDs: Theoretical Study Within DFT Framework (GVJ-2e Method), (2017).
31. *Seunghyun L., Zhaohui Z.* Nanoelectronic circuits based on two-dimensional atomic layer crystals.
32. Nanoscale 6, 13283-13300 (2014)
33. *McKone, J. R., Pieterick, A. P., Gray, H. B. & Lewis, N. S.* Hydrogen Evolution from Pt/Ru-Coated p-Type WSe 2 Photocathodes. J. Am. Chem. Soc. 135, 223–231 (2013).
34. *Zhang, F. et al.* Carbon doping of WS_2 monolayers: Bandgap reduction and p-type doping transport. Science Advances, 5(5), (2019).
35. *Q.H. Wang et al.* Electronics and optoelectronics of two-dimensional transition metal dichalcogenides. Nat. Nanotechnol., 7, pp. 699-712 (2012).
36. *Tingting Xu et al.* The ultra-high NO2 response of ultra-thin WS_2 nanosheets synthesized by hydrothermal and calcination processes. Sensors and Actuators B: Chemical, Volume 259, Pages 789-796 (2019).
37. *Cong. C.X. et al.* Optical properties of 2D Semiconductor WS_2. Advanced Optical Materials 6, 1700767 (2018).
38. *Yingdong Han et al.* Solution processable transition metal dichalcogenides-based hybrids for photodetection. Nano Materials Science, Volume 1, Issue 4, Pages 288-298 (2019).
39. *G. Lucovsky, V. Misra.* Thermal Chemical Vapor Deposition. Encyclopedia of Materials : Science and Technology (2018).
40. *C. Tan et al.* Non-volatile resistive memory devices based on solution-processed ultrathin two-dimensional nanomaterials. Chem. Soc. Rev., 44 (9), pp. 2615-2628 (2015).

41. *Y. Wang et al.* Solution-processed MoS_2/Organolead trihalide perovskite photodetectors. Adv. Mater., 29 (4), p. 1603995 (2017).
42. *Coleman, J. N.* Liquid Exfoliation of Defect-Free Graphene. Acc. Chem. Res. 46, 14–22 (2013).
43. *Backes, C. et al.* Guidelines for Exfoliation, Characterization and Processing of Layered Materials Produced by Liquid Exfoliation. Chem. Mater. 29, 243–255 (2017).
44. *Niu, L. et al.* Production of Two-Dimensional Nanomaterials via Liquid-Based Direct Exfoliation. Small, 12: 272-293 (2016).
45. *Yin, Z. et al.* Au Nanoparticle-Modified MoS_2 Nanosheet-Based Photoelectrochemical Cells for Water Splitting. Small, 10: 3537-3543 (2014)
46. *Li, Y. et al.* Electrochemical Intercalation in Atomically Thin van der Waals Materials for Structural Phase Transition and Device Applications. Adv. Mater. 33, 2000581 (2021).
47. *Lin, Z et al.* Solution-processable 2D semiconductors for high-performance large-area electronics. Nature 562, 254–258 (2018).
48. *Takashi Yanase et al.* Healing Sulfur vacancies in monolayer MoS_2 by high-pressure sulfur and Selenium annealing: implication for high-performance transistors. ACS Applied Nano Materials 2020 3 (10), 10462-10469
49. *J. Durán et al.* Charge carrier injection and transport engineering in two-dimensional transition metal dichalcogenides. Chem. Sci. ,9, 7727-7745 (2018).
50. *Mengge, Li et al.* P-type doping in Large-Area Monolayer MoS_2 by chemical vapor deposition. ACS Appl. Mater. Interfaces 12, 5, 6276–6282 (2020)
51. *Gupta, P., Rahman, A., SubRamanian, S. et al.* Layered transition metal dichalcogenides: promising near-lattice-matched substrates for GaN growth. Sci Rep 6, 23708 (2016).
52. *Saptarshi D. et al.* Nb-doped single crystalline MoS_2 field effect transistor. Applied Physics Letters 106, 173506 (2015)
53. *Sun Y.C. et al.* Effect of Nb doping on chemical sensing performance of two dimensional layered $MoSe_2$. ACS Appl. Mater. Interfaces 9, 4, 3817–3823 (2017).
54. *Lin, D.Y.; Jheng, J.J.; Ko, T.S.; Hsu, H.P.; Lin, C.F.* Doping with Nb enhances the photoresponsivity of WSe_2 thin sheets. AIP Adv. 8, 055011 (2018)
55. *Hung-Pin Hsu et al.* High Optical Response of Niobium-Doped WSe_2-Layered Crystals. Materials 12(7), 1161 (2019).
56. *A. R. Kim et al.* Alloyed 2D Metal-Semiconductor Atomic Layer Junctions. Nano Lett. 16, 1890 (2016).
57. *Sushil Kumar Pandey et al.* Controlled p-type subsitutional doping in large-area monolayer WSe_2 crystals grown by chemical vapor deposition. Nanoscale, 10, 21374-21385 (2018).
58. *K. Dolui et al.* Possible doping strategies for MoS_2 monolayers. Phys. Rev. B 88(7), 075420 (2013).
59. *K. K. Tiong et al.* Growth and characterization of Rhenium-doped MoS_2 single crystals Cryst. Growth 205(4), 543 (1999).
60. *Hallam, T. et al.* Rhenium-doped MoS_2 films. Appl. Phys. Lett. 111, 203101 (2017)

61. *Debjit Ghoshal et al.* Controlled Re doping in MoS_2 by chemical vapor deposition. Inorganic Chemistry Communications, Volume 123, 108329 (2021).

62. *Yuanyuan, L.* Effect of Rhenium dopants on photocarrier dynamics and optical properties of monolayer, few-layer and bulk MoS_2. Royal Society of Chemistry, Vol 7, 101039 (2020)

63. *Yang, S.-Z. et al.* Rhenium-doped and stabilized MoS_2 atomic layers with basal-plane catalytic activity. Adv. Mater. 30, 1803477 (2018)

64. *In Su Jeon et al.* One-step synthesis of Zn-doped MoS_2 nanosheets with tunable doping concentration using dopants-loaded seeding promoters for visible-light flexible photodetectors. Journal of Alloys and Compounds, Volume 835, 155383 (2020)

65. *Dong-Ho Kang et al.* Nondegenerate n-type doping phenomenon on molybdenum disulfide (MoS2) by zinc oxide (ZnO). Materials Research Bulletin, Volume 82, Pages 26-30 (2016).

66. *Peitao Liu et al.* Active basal plane catalytic activity and conductivity in Zn doped MoS2 nanosheets for efficient hydrogen evolution. Electrochimica Acta, Volume 260, Pages 24-30 (2018).

67. *G. Eda , H. Yamaguchi , D. Voiry , T. Fujita , M. Chen and M. Chhowalla*. Photoluminescence from Chemically Exfoliated MoS_2, Nano Lett., 11 , 5111 —5116 (2011)

68. *Cunningham, G. et al.* Solvent Exfoliation of Transition Metal Dichalcogenides: Dispersibility of Exfoliated Nanosheets Varies Only Weakly between Compounds ACS Nano, 6, 3468– 3480 (2012).

69. *Coleman, J. N.* Liquid Exfoliation of Defect-Free Graphene Acc. Chem. Res. 46, 14– 22 (2013).

70. *Sanjib Biswas and Lawrence T. Drzal.* A novel approach to create a highly ordered monlayer film of graphene nanosheets at the liquid-liquid interface. Nano Letters 9 (1), 167-172 (2019).

71. *Yu, X. et al.* Self-assembled 2D WSe_2 thin films for photoelectrochemical hydrogen production. Nat Commun 6, 7596 (2015).

72. *Joonki Suh et al.* Doping against the native propensity of MoS_2: Degenerate hole doping by cation substitution. Nano Letters 14 (12), 6976-6982 (2014).

73. *B. Morosin et al.* Structure refinement on NbS_2. Acta Cryst. B30, 551-552 (1974)

74. *Bernardi, M. et al.* Extraordinary sunlight absorption and one nanometer thick photovoltaics using two-dimensional monolayer materials. Nano Lett. 13, 3664–3670 (2013).

75. *Tan, M. X. et al.* Principles and Applications of Semiconductor Photoelectrochemistry. Progress in Inorganic Chemistry, Wiley-Blackwell, 21–144 (2007).

76. *Kuraganti V. et al.* Manganese doping of $MoSe_2$ promotes active defect sites for hydrogen evolution. ACS Appl Mater Interfaces 11: 25155– 25162 (2019).

77. *Martinez LM. et al.* Magnetic and electrocatalytic properties of transition metal doped MoS_2 nanocrystals. J Appl Phys 124:153903 (2018).
78. *Francis Oliver Vinay Gomes et al.* High mobility solution processed MoS_2 thin film transistors. Solid-State Electronics, Volume 158, Pages 75-84 (2019).
79. *Amirhasan Nourbakhsh et al.* MoS_2 field-effect transistor with sub-10 nm channel length. Nano Lett. 16, 12, 7798–7806 (2016).
80. *Tong X, et al.* Advances in MoS_2-Based Field Effect Transistors (FETs). Nanomicro Lett.;7(3):203-218 (2015)
81. *Xiaoyun Yu. et al*. Multiflake thin film electronic devices of solution processed 2D MoS_2 enabled by sonopolymer assisted exfoliation and surface modification. Chem. Mater. 26, 20, 5892–5899 (2014).
82. *Vivek Mootheri et al.* Understanding ambipolar transport in MoS_2 field effect transistors: the substrate is the key. Nanotechnology, 32, 135202 (2021).
83. *Jiaojiao Song et al.* Fabrication of solution-processed ambipolar electrolyte-gated field effect transistors form a MoS_2-polymer hybrid for multifunctional optoelectronics. J. Mater. Chem. C, 9, 1701-1708 (2021)
84. *Y. Jin et al.* Synthesis and transport properties of degenerate p-type Nb-doped WS_2 monolayers. Chem. Mater. 31, 9, 3534–3541 (2019).
85. *Shogo Sasaki* et al. Growth and optical properties of Nb-doped WS_2 monolayers. Appl. Phys. Express 9 071201 (2016)
86. *David Tuschel.* Effect of dopants or impurities on the RAMAN spectrum of the host crystal. Spectroscopy, Volume 32, Issue 12, Pages 13-18, 24 (2017).
87. *Rathod, Priyanshu et al.* Extrinsic p-type doping of few layered WS_2 films with niobium by pulsed laser deposition. Applied Physics Letters. 113. 062106 (2018).
88. *Fang Wang et al.* Strain-induced phonon shifts in tungsten disulfide nanoplatelets and nanotubes. 2D Mater. 4, 015007 (2017).
89. *Yuanyuan Li.* et al. Effects of Rhenium dopants on photocarrier dynamics and optical properties of monlayer, few layer and bulk MoS_2. Nanoscale, 9, 19360-19366 (2017).
90. *Guoping Gao et al.* Charge mediated semiconducting-to-metallic phase transition in Molybdenum Disulfide Monolayer and Hydrogen evolution reaction in new 1T' phase. J. Phys. Chem. C. 119, 23, 13124-13128 (2015).
91. *Andres Castellanos-Gomez et al.* Spatially resolved optical absoprtion spectroscopy of single and few-layer MoS_2 by hyperspectral imaging.
92. *Meiying Liang et al.* Improving stability of organometallic-halide perovskite solar cells using exfoliation two-dimensional molybdenum chalcogenides. 2D Materials and Applications 4, 40 (2020).